Centro de Investigaciones en Óptica, A.C. &
University of Dayton

Direct Observation of Conservation of OAM in Type-I Collinear SPDC

T H E S I S

In Partial Fulfillment of the Requirements for The Degree:

Master in Science

PRESENTS:

Carlos Andrés Sevilla Gutiérrez

ADVISOR:
Dr. Roberto Ramírez Alarcón
Dr. Qiwen Zhan

León, Guanajuato, October 2018

Acknowledgements

I would like to express my gratitude to my advisor at CIO, Roberto Ramírez Alarcón, for allowing me to be part of his group and for the help and advice in many aspects related and unrelated to my thesis project. Also to my advisor at the University of Dayton, Qiwen Zhan, for receiving me into his group, for his guidance and patience during my stay at UD, and apart from being a great advisor, he is a great teacher. I would like to acknowledge my group partners, especially to Zeferino Ibarra Borja, who was my biggest support in my thesis project, in and out the laboratory. And finally but not less important, to my family, who showed me their support in other ways and had to stand me in my most stressful moments.

I am very grateful to CONACYT for granting me a scholarship during my Master studies, along with an additional scholarship (Beca Mixta) for my studies abroad. Moreover their additional support given through the project C-469/2018 granted to CIO for the realization of: **Dual Master and Doctorate Programs between University of Dayton and Centro de Investigaciones en Óptica, A.C (CIO).**

Abstract

We implement a direct measurement of the spatial modes distribution generated in a collinear type I spontaneous parametric down-conversion (SPDC) process using a triggered ICCD camera. This type of experiments have been realized previously. However such those cases the measurement was an indirect one, where both photons were collected into one-pixel detectors. In this thesis, to the best or our knowledge, it is the first time that a direct two dimensional measurement of the spatial modes distribution is made. These are well described by Laguerre-Gaussian modes. In our experiments we could observe up to mode $l = \pm 10$. By exploiting the capabilities of an ICCD camera, it is possible to visualize the orbital angular momentum (OAM) conservation of the unprocessed SPDC bi-photon state. This is performed by observing the diffraction pattern by a triangular aperture. We show the results using this method for modes $l = \pm 1, \pm 2$. This conservation of OAM leads to entanglement in OAM, since one photon carries the anti-correlated topological charge with respect to the other one. Therefore, they are conditioned to the state of the other photon.

Contents

Abbreviations

APD Avalanche photodiode

AS Angular spectrum

BBO Beta barium borate

CAS Conditional angular spectrum

CCD Charge-coupled device

HWP Half wave plate

ICCD Intensified charge-coupled device

IP Image plane

JSA Joint spectral amplitude

LG Laguerre-Gauss

NIM Nuclear instrumentation module

OAM Orbital angular momentum

QKD Quantum key distribution

QWP Quarter wave plate

SLM Spatial light modulator

SMF Single mode fiber

SPDC Spontaneous parametric down-conversion

TA Triangular Aperture

Chapter 1

Introduction

1.1 Motivation

In 1992, L. Allen *et. al.* [1], showed that light beams with a helical phase-front carry orbital angular momentum (OAM). Since then, this topic has become an active research area given its broad field of application, such as optical trapping, imaging, optical communications, etc [2]. Especially in optical communications [3], since orbital angular momentum represent a basis of theoretically infinite dimension. This is a tremendous advantage in comparison with other degrees of freedom, such as the polarization, which is a binary basis.

Since a photon can carry well defined OAM, it has been studied and proposed for the implementation of quantum key distribution (QKD) protocols. QKD is a technique that revolves around the Heinsenberg Principle in quantum mechanics, which states that any measurement made on the system will modify the system. Such a quantum behavior is useful in cryptography for the detection of an eavesdropper.

The first protocol, was proposed in 1984 by C. Bennet and G. Brassard [4], known as the BB84 protocol, which uses photon polarization states. Recently it was published the first satellite-relayed intercontinental quantum network using these states [5], connecting two parties separated 7600 km away from each other. Other protocols that benefit from different features of the chosen quantum state, have also been proposed and explored. But nevertheless, having a higher dimensional state that can increase the information transmission rate per photon is highly desired.

QKD protocols for higher dimensional states using OAM have have attracted significant attention [6]. Using the entanglement of photons for QKD, the security of the message can be increased even more against eavesdropping, using Bell tests as an indicator [7]. More exotic states have been developed using a hybrid entanglement between polarization and OAM [8]. More recently investigated, the entanglement of complex

structured photons, that are the superposition of states with different OAM modes and polarizations [9]. These have been also implemented in both, controlled environment inside the laboratory [10] and outside the laboratory in a real life environment [11] [12] to study the effect of a turbulent atmosphere on the photon state.

This thesis lays the foundation of all mentioned above. It is a qualitative study of a fundamental process that is very interesting and important to investigate given its potential applications. We study and implement a source that intrinsically generates pairs of entangled photons in OAM, via spontaneous parametric down conversion (SPDC), specifically for type-I in collinear configuration. We will prove that the OAM in such process is conserved, by doing a direct measurement of the photonic state. Although this experiment has been done a couple of times earlier [10][13], performing a indirect measurement collecting both photons with one-pixel detectors, this is the first time, to the best of our knowledge, that a two-dimensional detector (ICCD camera) is used[14]. This makes possible the observation of the spatial distribution and the topological charge of the photons.

1.2 Objectives

The main objective of this thesis is to study the spatial correlations between the pair of photons generated via type-I SPDC, that rule the conservation in orbital angular momentum. To this end, we will implement a setup that will let us observe the spatial modes carrying OAM in this non-linear optical phenomenon, and be able to measure the topological charge of such modes. Finally, we will observe and analyze the mechanism of orbital angular momentum conservation which leads to the generation of entangled pairs of photons in such degree of freedom.

With these in mind, we will develop and learn the necessary techniques to generate pair of photons entangled in orbital angular momentum, and move forward to its possible applications in the field of quantum communications.

1.3 Thesis Structure

The content of this thesis is divided into 3 chapters. The first one corresponds to the theoretical background needed to study the phenomenon: classical light carrying OAM and its detection, nonlinear optical phenomena, geometrical and quantum description of SPDC, and finally conservation of OAM in type-I SPDC. The second chapter will show the optical set-ups to carry out the experiment. Finally, in the last one, we will present and analyze the results, and describe the future research work.

Since we are interested in the propagation of these OAM modes in free space for optical communications, in the appendix it is described the methodology that we will follow in our future research work considering a turbulent atmosphere, although so far it's been done only for classical scalar and vectorial vortex beams.

Chapter 2

Theory

In this chapter we will briefly describe the theoretical background needed to understand the subject of the thesis.

2.1 Wave Equation

All the description of Classical Electrodynamics is enclosed in Maxwell's equations, which are given below for the case of no free charges and currents:

$$\vec{\nabla} \times \tilde{\mathbf{E}} = -\frac{\partial}{\partial t}(\mu \tilde{\mathbf{H}}), \tag{2.1}$$

$$\vec{\nabla} \times \tilde{\mathbf{H}} = \frac{\partial}{\partial t}(\epsilon \tilde{\mathbf{E}}), \tag{2.2}$$

$$\vec{\nabla} \cdot \epsilon \tilde{\mathbf{E}} = 0, \tag{2.3}$$

$$\vec{\nabla} \cdot \mu \tilde{\mathbf{H}} = 0. \tag{2.4}$$

From these equations, we can derive the expression that tells us how electromagnetic radiation propagates in space, that turns out to be in the form of a wave [15]:

$$\nabla^2 \tilde{\mathbf{E}} - \mu\epsilon \frac{\partial^2}{\partial t^2} \tilde{\mathbf{E}} = 0. \tag{2.5}$$

All the information of the medium of propagation is given by the permittivity, ϵ, and the permeability, μ, since they are related to the electric and magnetic susceptibilities of the medium, χ_e and χ_m, through:

$$\begin{aligned} \epsilon &= \epsilon_0 \epsilon_r = \epsilon_0 (1 + \chi_e), \\ \mu &= \mu_0 \mu_r = \mu_0 (1 + \chi_m), \end{aligned} \tag{2.6}$$

where ϵ_r and μ_r are the relative permittivity and permeability, respectively. The susceptibilities are parameters that can be spatial and frequency dependent and express how the medium is going to respond to the electromagnetic field, and this interaction is in the form of a induced Polarization, $\tilde{\mathbf{P}}$, or Magnetization, $\tilde{\mathbf{M}}$ and are given by:

$$\tilde{\mathbf{P}} = \epsilon_0 \chi_e \tilde{\mathbf{E}}, \tag{2.7}$$

$$\tilde{\mathbf{M}} = \chi_m \tilde{\mathbf{M}}. \tag{2.8}$$

Another useful relation is the one between the susceptibility and the refractive index. From Eq. (2.5) we can see that $\frac{1}{\epsilon\mu}$ is the velocity of the light in the medium, u^2, and we know that $\frac{1}{\epsilon_0\mu_0}$ is the speed of light in the vacuum, c, so for a paramagnetic medium ($\mu_r = 1$) the refractive index n is:

$$n = \sqrt{\epsilon_r} = \sqrt{1 + \chi_e}. \tag{2.9}$$

2.1.1 Scalar Helmoltz Equation and Paraxial Approximation

Assuming a field that is polarized in one component $\tilde{\mathbf{E}} = E_i \hat{e}_i$, writing it as a multiplication of its spatial and temporal parts, $E_i = T(t)\xi(r)$ and plugging it in Eq.(2.5) is straight forward to show that the temporal dependence of the electric field is:

$$T(t) = e^{i\omega t}, \tag{2.10}$$

while the spatial dependence part, $\xi(r)$, is the solution of the time independent wave equation, also called the *scalar Helmholtz equation*:

$$\nabla^2 \xi(r) + k^2 \xi(r) = 0, \tag{2.11}$$

where k is the wave number defined as $k = n\omega/c$, and also is the magnitude of the propagation vector $\vec{\mathbf{k}}(k_x, k_y, k_z)$ of the wave.

Now, applying the paraxial approximation, that is, assuming that the propagation of the wave is predominantly along the optical axis (chosen to be the z-axis), we can write ξ as:

$$\xi(r) = u(r)e^{-ikz}. \tag{2.12}$$

Substituting this in Eq. (2.11) and applying the Slowly Varying Envelope Approximation (SVEA) in the z direction, which is:

$$\left|\frac{\partial^2 u}{\partial z^2}\right| \ll k\left|\frac{\partial u}{\partial z}\right|, \tag{2.13}$$

Eq. (2.11) becomes:

$$\nabla_t{}^2 u(r) + 2ik\frac{\partial u(r)}{\partial z} = 0. \tag{2.14}$$

2.1.2 Families of Solutions of the Paraxial Helmholtz Equation

The Helmholtz equation in the paraxial regime can be solved exactly depending on the physical symmetry. For rectangular symmetry, we can separate the two transversal components x and y as:

$$u_{nl}^{HG}(x, y, z) = u_n^{HG}(x, z)u_m^{HG}(y, z), \tag{2.15}$$

and obtain a solution for each one that is the product of a Gaussian with a Hermite polynomial, and it is called a Hermite-Gauss (HG) beam:

$$u_n^{HG}(x, z) = \frac{\sqrt{1/(2^n n!)}(2/\pi)^{1/4}}{\sqrt{w(z)}} e^{ik\frac{x^2 z}{2(z_R^2+z^2)}} e^{-\frac{x^2}{w^2(z)}} e^{-i(n+\frac{1}{2})\psi_g(z)} H_n\Big(\frac{\sqrt{2}x}{w(z)}\Big), \tag{2.16}$$

where n is the hermite polynomial order, $w(z)$ is the beam waist. Z_R is the Rayleigh length and $(n+\frac{1}{2})\psi_g(z)$ is the *Gouy phase*. The latter expression is given by:

$$\Psi_g(z) = tan^{-1}\frac{z}{z_R}. \tag{2.17}$$

In the first row of Fig. 2.1 HG modes are simulated for different values of n and m. Here the number of lobes in the x-direction is given by $(m+1)$ and similarly for the y-direction, the modes have $(m+1)$ lobes.

Now, for cylindrical symmetry, the solution is given as a multiplication of a Gaussian with a generalized Laguerre polynomial. This is known as a Laguerre-Gauss (LG) beam and it is described by the following equation [15]:

$$u_{lp}^{LG}(\rho, \phi, z) = \frac{C_{lp}^{LG}}{\sqrt{w(z)}}\Big(\frac{\rho\sqrt{2}}{w(z)}\Big)^{|l|} e^{-\frac{\rho^2}{w^2(z)}} L_p^{|l|}\Big(\frac{2\rho^2}{w^2(z)}\Big) e^{-ik\frac{\rho^2 z}{2(z_R^2+z^2)}} e^{-i(2p+|l|+1)\psi_g(z)} e^{il\phi}. \tag{2.18}$$

Here, l and p are the azimuthal and radial indexes, $(2p+|l|+1)\psi_g(z)$ is the Gouy phase for this case and C_{lp}^{LG} is the normalization constant equal to $C_{mp}^{LG} = \sqrt{\frac{2^{|m|+1}p!}{\pi(p+|m|)!}}$. The second row of Fig. 2.1 show LG modes for different values of p and l. From these modes we can see that the number of rings is $p+1$ and that the radius increases monotonically with $|l|$.

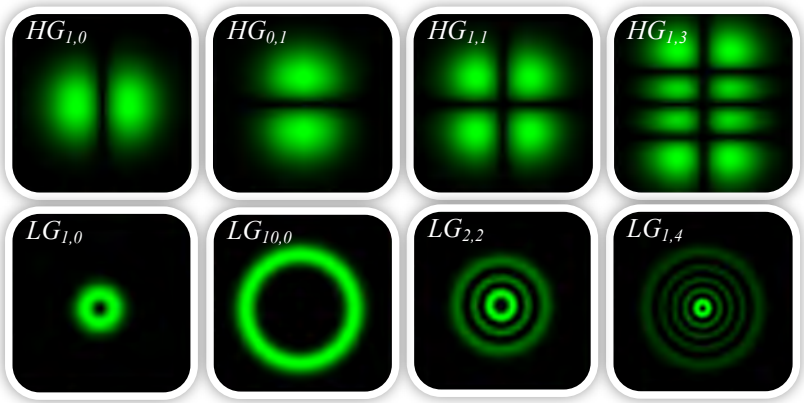

Figure 2.1: First row displays HG modes for different values of n and m. Second row displays LG modes for different values of l and p.

Laguerre-Gaussian modes form a complete set of orthonormal modes in the azimuthal index l when integrated over ϕ, and also in the radial indexes when integrated over ρ, that is:

$$\int_0^{2\pi} d\phi \int_0^{\infty} \rho d\rho [u_{lp}^{LG}(\rho, \phi, z)][u_{l'p'}^{LG}(\rho, \phi, z)]^* = \delta_{pp'}\delta_{ll'}. \tag{2.19}$$

Hermite-Gaussian modes are also orthonormal in m and n, when integrated over x and y, respectively. As both of these modes form bases, one can write an arbitrary EM field as a super position of HG or LG modes.

2.1.3 Light Beams Carrying Orbital Angular Momentum

The Orbital Angular Momentum of a wave is associated with a spiral wave front, where the number of intertwined twists l, in a distance λ is the quantity of OAM carried by the beam. This is also called *topological charge*. Figures 2.2 (a-b) show spiral wave fronts for different values of l. Here the sign of the topological charge defines the rotation direction of the wave front.

We note from Eq. (2.18) that LG beams have well defined OAM by looking at the phase dependence $e^{il\phi}$. Photons belonging to such beams are said to have $l\hbar$ units of OAM.

Beams with OAM are characterized by a ring-shape transversal intensity with zero intensity along the optical axis (see Fig. 2.2(c)), which is the reason they are also

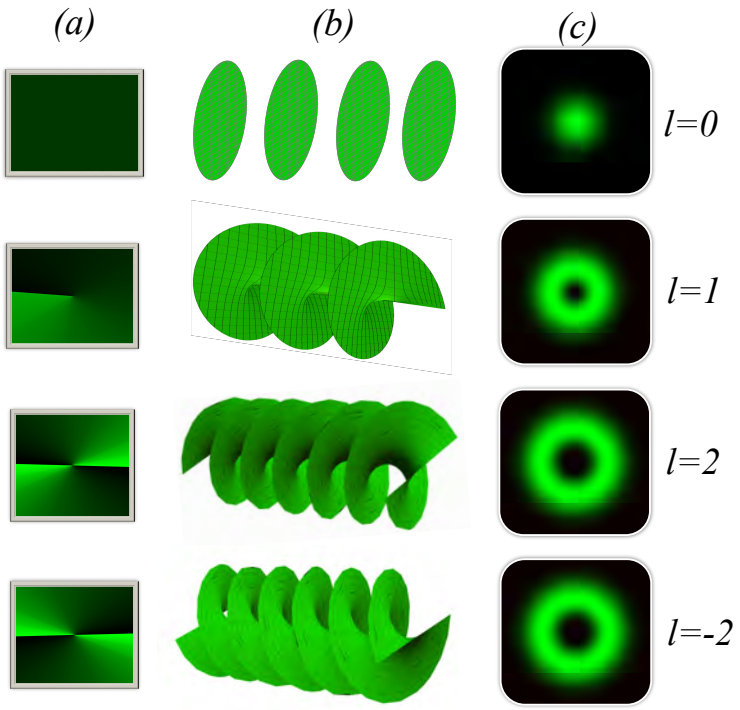

Figure 2.2: (a) Two-dimensional phase-front, that corresponds to a phase from 0(dark part) to 2π (bright part), (b) three-dimensional wavefront and (c) transversal intensity amplitude of beams carrying OAM.

referred as a kind of *Cylindrical Vortex beams*. This arises from the phase singularity, since the electric field needs to be continuous, it is modulated to reach zero at the center.

To transfer OAM it is necessary to project the phase $e^{il\phi}$ onto the wave. This can be done easily by using a Spatial Light Modulator (SLM). A SLM is a small screen divided in pixels, where each pixel is an independent birefringent liquid crystal that by applying a certain voltage V, the orientation of the optical axis of the liquid crystal is rotated and, in this way, the refractive index for the extraordinary polarization changes. Thus, the desired phase modulation can be done from point to point (pixel to pixel). A schematic is shown in Fig. 2.3.

2.1.4 OAM Direct Measurement from the Diffraction Pattern by a Triangular Aperture

From the ring-shape intensity profile of the beam carrying OAM, we do not get much information related to the topological charge, except for the radius of the ring, which

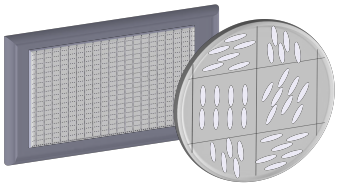

Figure 2.3: Schematic of a SLM, showing a different rotation of the optical axis in each pixel, thus, a different phase modulation per pixel.

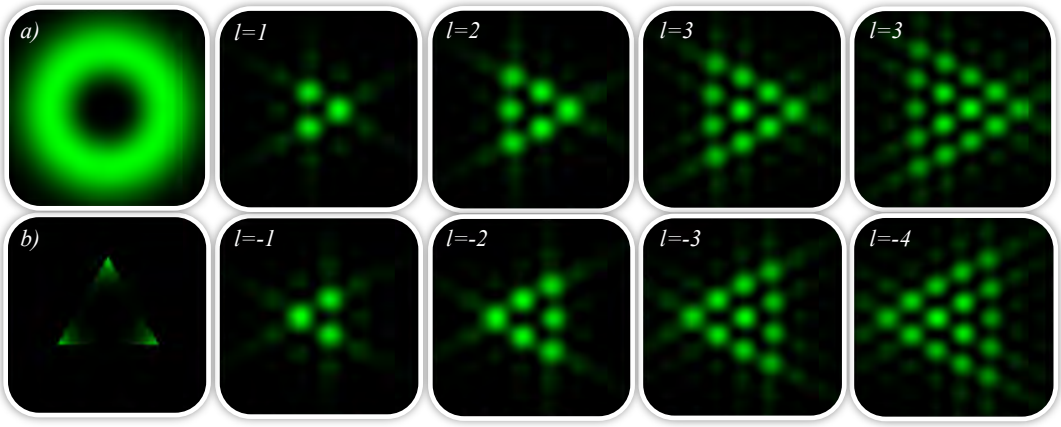

Figure 2.4: (a)Beam with ring-shaped transversal intensity profile with arbitrary topological charge. (b)Binary amplitude mask with shape of an equilateral triangle applied to the same beam. The following figures show the diffraction pattern of (b) in the far-field with OAM from $l = \pm 1$ to $l = \pm 4$.

increases as $|l|$ increases, but this is not useful if we do not have any information of the beam prior to measure it. Also there is no distinction between l and the anti-correlated charge $-l$.

The OAM is encoded in the phase, meaning that we need to resort to interferometric or other methods, than can be more bulky and tedious. An easier way to observe the topological charge directly is by looking at the diffraction pattern formed in the far field by a triangular aperture [16]. When a beam with ring-shaped intensity profile passes through an aperture of this kind, the Fraunhofer diffraction pattern is conformed by circular spots arranged in a triangular manner as shown in Fig. 2.4, where the topological charge can be directly observed being $l = N - 1$, where N is the number of spots per side. This triangular shaped agglomeration of circular spots is rotated $\pm\frac{\pi}{6}$ with respect to the triangular aperture, and the sign of the rotation gives away the sign of the OAM.

2.2 Non-Linear Optics

In section 2.1 we discussed about the response of the medium to the interaction with an external electric field, given by:

$$\tilde{\mathbf{P}}(t) = \epsilon_0 \chi \tilde{\mathbf{E}}(t). \tag{2.20}$$

This induced polarization is linear with the incident electric field. However can be generalized by expanding it in a power series to consider non-linear dependencies with the E field:

$$\tilde{\mathbf{P}}(t) = \epsilon_0 \left[\chi^{(1)} \tilde{\mathbf{E}}(t) + \chi^{(2)} \tilde{\mathbf{E}}^2(t) + \chi^{(3)} \tilde{\mathbf{E}}^3(t) + ... \right]. \tag{2.21}$$

Here, $\chi^{(1)}$ is called the linear susceptibility, $\chi^{(2)}$ and $\chi^{(3)}$ are the non-linear susceptibilities of second and third order, respectively. We can define the second order non-linear polarization as:

$$\tilde{\mathbf{P}}(t)^{(2)} = \epsilon_0 \chi^{(2)} \tilde{\mathbf{E}}^2(t) \tag{2.22}$$

Non-linear processes are highly inefficient, $\chi^{(2)}$ being of the order 10^{-12}. Therefore an intense electric field is needed to observe non-linear optical phenomena and they are only present in non-centrosymmetric media, where, the electronic potential is not symmetric [17].

There are different second order nonlinear processes that are described below. Let us assume that the incident electric field as a sum of different frequencies, which can be expressed as:

$$\tilde{\mathbf{E}} = \hat{e}_i \sum_{n=1}^{N} (E_n e^{-i\omega t} + E_n^* e^{i\omega t}). \tag{2.23}$$

Substituting this field in Eq. 2.22 we note that the polarization terms oscillate $\omega = \pm(\omega_n \pm \omega_m)$. Depending on the sign we choose different second-nonlinear processes are defined.

For the case $n = m$ we obtain *second harmonic generation* (SHG) if we choose the positive sign, where a field with an oscillation frequency $\omega = 2\omega_n$ is created. While if we choose the negative sign, we obtain *optical rectification* OR, with frequency $\omega = 0$.

Similarly, for the case $n \neq m$ we obtain *sum frequency generation* (SFG) by choosing the positive sign, $\omega = \pm(\omega_n + \omega_m)$, and *difference frequency generation* (DFG), by choosing the negative sign, $\omega = \pm(\omega_n - \omega_m)$.

All these processes in theory can take place but the amplitude of generation of each is weighted by a function $\Phi(L\Delta_k)$, where L is the crystal length and:

$$\Delta_k = \mathbf{k}(\omega_n \pm \omega_m) - \mathbf{k}(\omega_n) \mp \mathbf{k}(\omega_m) \quad for \quad \omega_n \geq \omega_m. \tag{2.24}$$

The term $\Phi(L\Delta_k)$, is called phase matching function because has its maximum value when $\Delta_k = 0$, and decreases rapidly as $|L\Delta_k|$ increases. Since all these different processes have different $\mathbf{k}(\omega_n \pm \omega_m)$, it is not likely than more of one take place efficiently.

2.2.1 Spontaneous Parametric Down-Conversion

Spontaneous parametric down conversion (SPDC) is another second order non-linear process than can be seen as the reverse of the SFG, where a photon of frequency ω_p is down converted into two photons of frequency ω_s and ω_i, where the subscripts p, s and i denote pump, signal and idler photons respectively.

This process obeys the same principles of the former non-linear processes discussed in the last subsection, namely, the energy and linear momentum conservation, or phase matching (Fig. 2.5.a):

$$\omega_p = \omega_s + \omega_i, \tag{2.25}$$

$$\vec{k_p} = \vec{k_s} + \vec{k_i}, \tag{2.26}$$

Also, a big difference between this process and the other mentioned above, is that SPDC is not restricted to a combination of the incident frequencies, since one photon from the pump beam can be down-converted into any pair of photons that meets the conservation requirements, the photonic variables (k_n,ω_i, k_n,ω_i) are continuous. Another difference is that SPDC, as stated in its name, is a spontaneous process since no other field stimulates the transition, except the vacuum fluctuations.

In this section we will only consider the case of type-I SPDC, where the pump photon is $\hat{e}$-polarized and the signal and idler photons are $\hat{o}$-polarized ($e \rightarrow o + o$) in a birefringent negative uniaxial crystal.

Fig. 2.6 (a) shows the geometrical description of SPDC [18], where we depict the pump wave vector $\vec{k_p}$,the extraordinary $\hat{e}$, ordinary $\hat{o}$ and the optical (OA) axes of the crystal, the latter lying on the $\vec{k_p} - \hat{e}$ plane forming an angle θ_p with $\vec{k_p}$. Since the pump has extraordinary polarization, the magnitude of its wave vector is also θ_p dependent ($k_p(\theta_p)$) through the following relation [17]:

$$\frac{1}{n_p^2} = \frac{\cos^2\theta_p}{n_o^2} + \frac{\sin^2\theta_p}{n_e^2}. \tag{2.27}$$

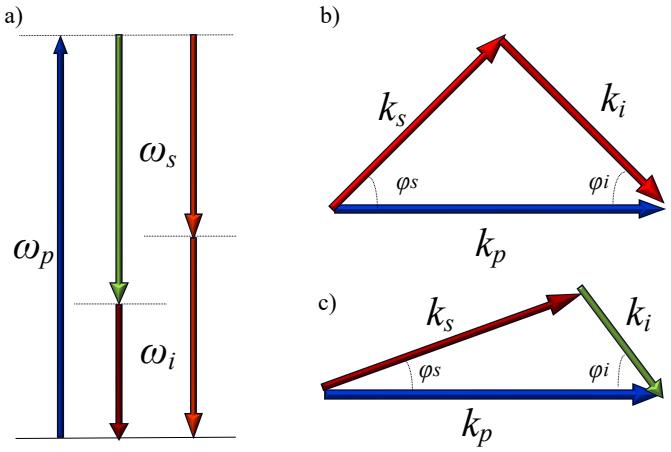

Figure 2.5: (a)Annihilation of a photon of frequency ω_p and creation of two photons of frequencies ω_s and ω_i showing energy conservation, (b) linear momentum conservation of the degenerate photons and (c) linear momentum conservation of the non-degenerate photons. Here ϕ_s and ϕ_i are the angle of propagation of the signal and idler photons

The idler and single photons are *o*-polarized, thus that the magnitude of their wave vectors are ϕ independent, where ϕ is the angle between the projection of k_s (red outlined arrow) with the $\hat{e}$-axis. Since this is not a restriction, cones are formed around k_p as shown in Fig. 2.6(b). The correlated pair of photons can be found by tracing an imaginary line from one extreme of the cone of the idler photon to the opposite extreme of the cone of the signal photon passing through the center as we can see in Fig. 2.6(c), where the three different matching figures represent sections of the rings that are correlated.

From Eq. (2.26) we can separate the longitudinal and transverse phase matching conditions, given respectively by the following set of equations [18]:

$$k_p(\theta_p) = k_s \cos\phi_s + k_i \cos\phi_i, \tag{2.28}$$

$$k_s \sin\phi_s = -k_i \sin\phi_i. \tag{2.29}$$

The emission angles(ϕ_{ei},ϕ_{es}) from the crystal for the idler and signal photons are given by the Snell equation:

$$\sin\phi_{ei} = n_i \sin\phi_i, \tag{2.30}$$

$$\sin\phi_{es} = n_s \sin\phi_s. \tag{2.31}$$

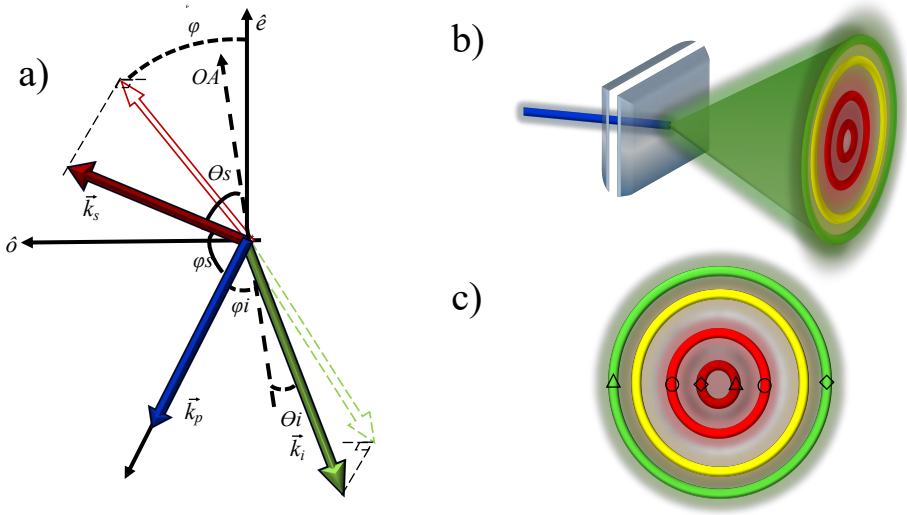

Figure 2.6: (a) Geometrical description of SPDC, (b) generation of concentric cones of different frequency ω and (c) the matching figures represent the sections of the rings that are correlated.

Using equations (2.28-2.31) and the Sellmeier equations to calculate $n_p(\lambda_p)$, $n_s(\lambda_s)$ and $n_i(\lambda_i)$, we can determine the emission angle for the idler and signal photons and we can control it by changing the orientation of the optical axis (θ_p). When we collapse it ($\phi_{es} \approx 0$,$\phi_{ei} \approx 0$) it is said to be *Type-I collinear SPDC*.

2.2.2 Quantum Description of SPDC

All the information of a quantum system is given by the wave function ψ, which is solution to the Schrödinger equation:

$$i\hbar \frac{\partial \psi(\mathbf{r}, t)}{\partial t} = \hat{H}\psi(\mathbf{r}, t). \tag{2.32}$$

Here, $\hat{H}$ is the Hamiltonian of the system, which has all the information about the interaction the of EM field with the matter. It can be written as:

$$\hat{H} = \hat{H}_0 + \hat{H}_I, \tag{2.33}$$

where $\hat{H}_0$ is the Hamiltonian for the free atoms of the crystal and $\hat{H}_I$ describes the interaction of the crystal with the EM field, and it is given by [19]:

$$\hat{H}_I = -\int dV \hat{P}\hat{E}_p, \tag{2.34}$$

with $\hat{P}$ being the polarization given in Eq. (2.20), and $\hat{E}_p$ the electric field pumping

the crystal. Since we are dealing with a second-order non-linear process we can keep only the second-order term from the Taylor series in Eq. (2.21), specially for the case $\pm(\omega_p - \omega_s - \omega_i) = 0$, thus:

$$\hat{P}\hat{E}_p = \epsilon_0 \chi^{(2)} \hat{E_i}^* \hat{E_s}^* \hat{E}_p + C.C. \tag{2.35}$$

Now, using the quantization of the electromagnetic field we can write the electric field operator in terms of the creation and annihilation operators[20]:

$$\hat{E_n}(\mathbf{r_n}, t) = i\mathbf{e_n}\left(\frac{\hbar\omega_m}{2\epsilon_0 v}\right)^{1/2} \int d\mathbf{k_n}\left[\hat{a_n} e^{(i\mathbf{k_n}\cdot r - \omega_n t)} - \hat{a_n}^\dagger e^{-(i\mathbf{k_n}\cdot r - \omega_n t)}\right]. \tag{2.36}$$

$$= \hat{E_n}^{(+)} + \hat{E_n}^{(-)}$$

The two-photon state of the system, in first order perturbation theory , is given by [21]:

$$|\psi\rangle = -\frac{1}{i\hbar}\int dt \hat{H_I} |1\rangle_p |0\rangle_s |0\rangle_i, \tag{2.37}$$

and writing it as a function of the electric field operators $\hat{E_n}^{(\pm)}$, we have:

$$|\psi\rangle = -\frac{\epsilon_0 \chi^{(2)}}{i\hbar}\int dt \int dV \hat{E_p}^{(+)} \hat{E_s}^{(-)} \hat{E_i}^{(-)} |1\rangle_p |0\rangle_s |0\rangle_i + H.C, \tag{2.38}$$

where H.C stands for hermitian conjugated. Here an approximation is made, taking into account the low efficiency of the SPDC ($\chi^{(2)} \approx 10^{-12}$ [17]), we approximate the pump field E_p in its classical form [22]:

$$E_p(r,t) = U(r) e^{i(k_p z - \omega_p t)}. \tag{2.39}$$

Here, $U(r)$ is the complex amplitude of the family solution to the paraxial Helmholtz equation. From Eqs. ((2.37)-(2.39)) the two-photon state is:

$$|\psi\rangle = -\frac{1}{i\hbar}\int d\mathbf{k_i} \int d\mathbf{k_s} \Phi(\mathbf{k_i}, \omega_i, \mathbf{k_s}, \omega_i) \hat{a_s}\hat{a_i} |0\rangle_s |0\rangle_i, \tag{2.40}$$

where,

$$\Phi(\mathbf{k_i}, \omega_i, \mathbf{k_s}, \omega_i) \propto \int dt \int d\omega_p \alpha(\omega_p) e^{i(-\omega_p + \omega_i + \omega_p)t} \int dV U(\mathbf{r}) e^{i(k_p - k_s^z - k_i^z)z - i(\mathbf{q_i} + \mathbf{q_s})\cdot\hat{\rho}}. \tag{2.41}$$

Here we have separated the wave vector, and position vector in their longitudinal and transversal parts $\mathbf{k_n} = k_n^z \hat{z} + \mathbf{q_n}$ and $\mathbf{r} = z\hat{z} + \hat{\rho}$ and $\alpha(\omega_p)$ being the temporal

broadband of the source. The function $\Phi(\mathbf{k_i}, \omega_i, \mathbf{k_s}, \omega_i)$ is called the *joint spectral amplitude* (JSA). The JSA term that works as weight function of the generation of the different pairs of photons in terms of their photonic parameters (ω_n, $\mathbf{k_n}$). It has all the information about the spatial, temporal, spatial-temporal correlations between the generated pair of photons. The modulus squared of $\Phi(\cdot)$ describes the spatial intensity distribution in momentum space of the SPDC. This is called *Angular Spectrum* (AS), when we are looking at the arrival of the individual photons which forms a incoherent superposition, and *Conditional Angular Spectrum* (CAS), when we look at the arrival of one photon conditioned to the partner's arrival, which is a coherent.

Another aspect to consider when calculating the JSA, is the *spatial walk-off*, which comes from the fact that the pump beam is propagating in a birefringent medium, and the energy flow, which is the Poynting vector $\vec{S}$, and the wavevector of the pump k_p deviate from each other. The angle between $\vec{S}$ and k_p, ρ_o, is defined as [23]:

$$\rho_o = -\frac{1}{n(\theta_p)} \frac{\partial n(\theta_p)}{\partial \theta_p}, \tag{2.42}$$

where θ_p is the angle between the optical axis and the polarization of the pump.

Assuming an incident a monochromatic elliptical Gaussian beam ($\alpha(\omega_p)$=$\delta(\omega_p - \omega_p 0)$) :

$$U(r) = \frac{1}{\sqrt{q_x(z)}} \frac{1}{\sqrt{q_y(z)}} e^{\frac{-x^2}{W_{0x} q_x(z)}} e^{\frac{-y^2}{W_{0y} q_y(z)}} e^{ik_p z} \tag{2.43}$$

where $q_n(z)$ is the *complex beam parameter* defined as:

$$q_n(z) = 1 - 2iz/(k_p W_{0_n}^2), \tag{2.44}$$

and no negligible walk-off on the $y-z$ plane, a crystal of length L, and that the x and y dimensions of the crystal are much larger than z, the integrals take the limits $-\infty < x < \infty$, $-\infty < y < \infty$, $-\frac{L}{2} < z < \frac{L}{2}$. The JSA for such system configuration is [23]:

$$\Phi(\mathbf{k_i}, \omega_i, \mathbf{k_s}, \omega_i) = L\pi W_{o_x} W_{o_y} e^{-\frac{1}{4}[(W_{ox} q_x \perp)^2 + (W_{oy} q_y \perp)^2]} \mathrm{sinc}\Big(\frac{L\Delta_{Keff}}{2}\Big), \tag{2.45}$$

where,

$$\begin{aligned}
\Delta_{Keff} &= q_y^{\perp} \tan\rho_0 - \Delta_{Kz}, \\
\Delta_{Kz} &= k_p^z - k_i^z - k_s^z, \\
k_p^z &= k_p - \frac{|q^{\perp}|}{2k_p}, \\
\mathbf{q}^{\perp} &= q_x^{\perp}\hat{x} + q_y^{\perp}\hat{y} = (q_i^x + q_s^x)\hat{x} + (q_i^y + q_s^y)\hat{y} = \mathbf{q_i} + \mathbf{q_s}.
\end{aligned} \tag{2.46}$$

2.2.3 Conservation of OAM in Type-I Collinear SPDC

We can usually express the JSA in a longitudinal part and a transversal part, the former is in the shape of a sinc function and the latter happens to have the distribution of the pump beam in momentum space $\mathcal{E}(\mathbf{q_i}, \mathbf{q_s})$, and it is a function of $q^{\perp}$, as we can see from Eq. (2.45):

$$\Phi(\mathbf{q_i}, \mathbf{q_s}) = \mathcal{E}(\mathbf{q_i}, \mathbf{q_s})\mathrm{sinc}\Big(\frac{L\Delta_{kz}}{2}\Big). \tag{2.47}$$

Regarding the sinc$(\cdot)$ function in the JSA, it depends on $|\mathbf{q}^{\perp}|$ through k_p^z. This can be expanded as:

$$|\mathbf{q}^{\perp}|^2 = |\mathbf{q_i} + \mathbf{q_s}|^2 = q_i^2 + q_s^2 + 2q_i q_s \cos(\phi_i - \phi_s). \tag{2.48}$$

Thus, performing Fourier analysis on $Sinc(\cdot)$, we can express it as[24]:

$$sinc(\frac{L\Delta_{Kz}}{2}) = \sum_{m=-\infty}^{\infty} F_m(q_i, q_s)e^{-im(\phi_i - \phi_s)}. \tag{2.49}$$

Now, assuming an incident pump beam carrying a topological charge l_p, in transverse momentum space, the distribution can be written as:

$$\mathcal{E}(q_i, q_s) = F(q^{\perp})e^{il_p\phi}, \tag{2.50}$$

where $\phi = \tan^- 1(\frac{q_y^{\perp}}{q_x^{\perp}})$. Using the relation $Ae^{i\phi} = A_x + iA_y$ and last line in Eq. (2.46) we can rewrite Eq. 2.50 as:

$$\mathcal{E}(q_i, q_s) = F(q^{\perp})[q_i e^{i\phi_i} + q_s e^{i\phi_s}]^{l_p}. \tag{2.51}$$

Finally, applying the binomial theorem:

$$(x+y)^n = \sum_{k=0}^{n} \binom{n}{k} x^k y^{n-k}, \tag{2.52}$$

then multiplying by Eq. (2.49), and grouping all the terms independent of $\phi_{i,s}$, we get [24]:

$$\Phi(\mathbf{q_i}, \mathbf{q_s}) = \sum_{l=0}^{l_p} \sum_{m=-\infty}^{\infty} F_m^l e^{i\{[l_p-(l+m)]\phi_i+(l+m)\phi_s\}} \tag{2.53}$$

$$= \sum_{l=-\infty}^{\infty} F_l e^{i\{(l_p-l)\phi_i+l\phi_s\}}. \tag{2.54}$$

From this expression we can see that the OAM from the pump is completely transferred to the pair of photon since the idler is generated with topological charge $l_i = l_p - l$ and signal with $l_s = l$. One can write a selection rule for OAM transfer which is:

$$l_p = l_i + l_s. \tag{2.55}$$

Eq. (2.55) holds when considering all the photons in the SPDC cone, but when only sections of the cones are considered, the selection rule does not necessarily hold. Reference [22] studies the case for different SPDC configurations, and shows how the smaller the pump waist and the larger the emission angle, and a no negligible walk-off, are detrimental factors in the selection rule fulfillment. Since we are working in collinear configurations, we take the selection rule as valid.

2.2.4 OAM Entanglement in Type-I Collinear SPDC

We can write our two photon state in any basis, and since we are interested in the OAM degree of freedom, we use a complete basis whose states are eigenstates of the OAM operator. As we discussed in section 2.1.2, LG modes gather these two requirements.

We can start by writing the individual state of each photon as a superposition of these modes:

$$\big|1\big\rangle_i \big|1\big\rangle_s = \Big(\sum_{l=-\infty,p=0}^{\infty} C_{lp} \big|Sp_l^p\big\rangle_i \Big)\Big(\sum_{l'=-\infty,p'=0}^{\infty} C_{l'p'} \big|Sp_{l'}^{p'}\big\rangle_s \Big). \tag{2.56}$$

Since we are only interested in the topological charge l of the photon, we can re-write the state as:

$$\begin{aligned} |1\rangle_i|1\rangle_s &= \Big(\sum_{l=-\infty}^{\infty} C_l|l\rangle_i\Big)\Big(\sum_{l'=-\infty}^{\infty} C'_l|l'\rangle_s\Big) \\ &= \sum_{l,l'=-\infty}^{\infty} C_l C'_l|l\rangle_i|l'\rangle_s. \end{aligned} \tag{2.57}$$

Here, $|l\rangle$ is the superposition of all the modes with same topological charge but different value of radial index p, which are called *spiral harmonic modes*:

$$C_l|l\rangle = \Big(\sum_{p=0}^{\infty} C_{lp}|Sp_l^p\rangle\Big). \tag{2.58}$$

The OAM selection rule (Eq. (2.55)) imposes a constriction in the system, making zero the coefficients $C_{lp}C_{l'p'} = 0$ when $l' \neq l_p - l$.

$$|\psi\rangle_{SPDC} = \sum_{l=0}^{\infty} \big(C_{l,l_p-l}|l\rangle|l_p - l\rangle + C_{l_p-l,l}|l_p - l\rangle|l\rangle\big). \tag{2.59}$$

The pair of photons generated are said to be entangled because the state (Eq. (2.59)) cannot be factorized as the multiplication of the individual photon states, since it would require to have non-vanishing coefficients $C_l C'_l \neq 0$.

Chapter 3

Experimental Characterization and Realization

In this chapter, the individual modules that consist the experiment are presented: SLM's gamma curve characterization, phase-mask generation for OAM transfer, generation of beams carrying OAM and direct measurement of the topological charge, type-I collinear SPDC source implementation. Finally, putting everything together, the setup used for observation of Spatial Modes carrying OAM in The Type I collinear SPDC, and the measurement of their topological charge.

3.1 SLM's Gamma Curve Characterization

The SLM used in these experiments is a HOLOEYE Pluto with a display of 1920×1800 pixels and a pixel pitch of $8\mu m$. It reads what is on the green channel of the computer's screen that is connected to it. The value of the phase is related to the value of the gray level read by the SLM. However, this is not linear and we need to characterize it.

The method we used [25] to calibrate the SLM, is to observe the output state of polarization (SOP) of the system in Fig. 3.1. This system is conformed by a quarter wave plate (QWP) with its fast axis at 45° with the horizontal, and a SLM placed parallel to the QWP with its extraordinary axis parallel to the horizontal.

A beam passing through this system impinging at normal incidence is going to see a QWP at 45°, a phase modulation($\delta(x, y)$) in the horizontal polarization component proportional to the $n_e(V) - n_o$, a reflection from the SLM, and finally, the same QWP but this time at 135°. Applying the Jones Matrix formalism, this system is described by:

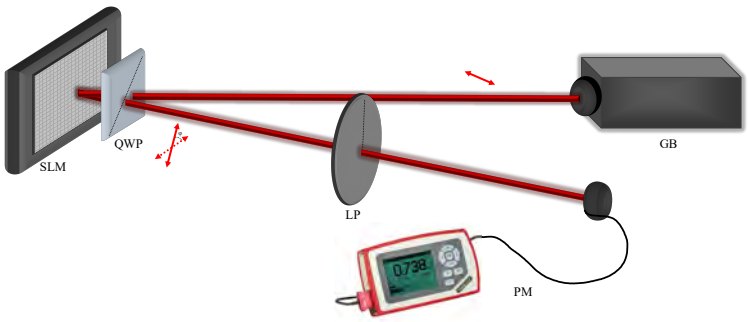

Figure 3.1: Setup for the SLM's Gamma curve characterization. (Powermeter picture taken from [26])

$$M = R(-3\pi/4)J_{QWP}R(-3\pi/4)\begin{pmatrix}-1 & 0\\ 0 & 1\end{pmatrix}J_{slm}R(\pi/4)J_{QWP}R(-\pi/4). \tag{3.1}$$

Performing this matrix multiplication we end up with [25]:

$$M = e^{i\delta(x,y)/2}\begin{pmatrix}-\sin\frac{\delta(x,y)}{2} & -\cos\frac{\delta(x,y)}{2}\\ \cos\frac{\delta(x,y)}{2} & -\sin\frac{\delta(x,y)}{2}\end{pmatrix}. \tag{3.2}$$

This matrix has the form of a rotation matrix by an amount of $\frac{\pi}{2} + \frac{\delta(x,y)}{2}$ with respect to the horizontal. We extract the phase value by measuring the polarization angle ϕ.

This characterization procedure is done, as in Fig. 3.1, for a wavelength $\lambda = 808nm$. The incidence angle on the SLM is small so that we can apply the above description. The polarization rotation is found using a power-meter and a linear polarizer, that is rotated θ radians, until we find a minimum intensity, which happens when $\theta = \frac{\pi}{2} + \frac{\delta(x,y)}{2} - \pi/2$. Thus, the phase is:

$$\delta(x, y) = 2\theta. \tag{3.3}$$

The value of the phase is found for different values of Gray level set in the SLM, until completing a period (0 to 2π) as shown in Fig. 3.2.

3.2 Phase Masks Generation for OAM Transfer

To transfer OAM to a beam it is necessary to multiply by a spiral phase $e^{il\phi}$, ϕ being the azimuthal angle given by:

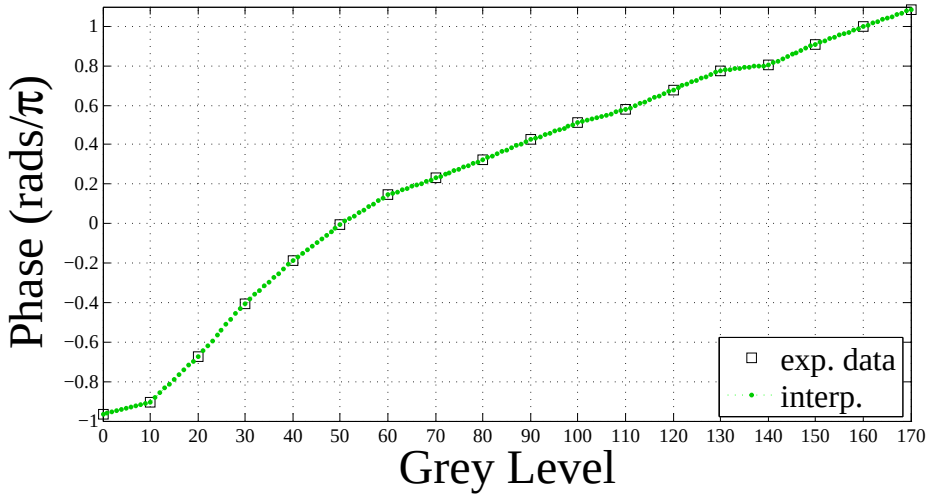

Figure 3.2: Phase vs. Grey Scale value. The squares are the experimental data and the green dashed line is the interpolation.

$$\phi(x, y) = atan(y/x) \tag{3.4}$$

Each value of $\phi(x, y)$ is substituted by the respective value of the gray scale found in the previous section and the image is generated in the green channel, since it is the one the SLM will read. In Fig. 3.3 are shown the phase-masks for the cases $l = \pm 1, \pm 2, \pm 5$ and ± 10.

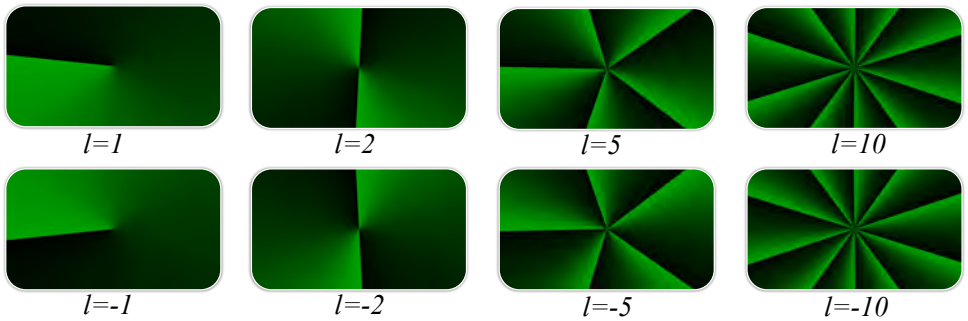

Figure 3.3: Phase masks used for the transfer of topological charge l.

3.3 Generation of Beams Carrying OAM and Observation of the Topological Charge

Figure 3.4(a) shows the optical array for the generation of beams with OAM, where a Gaussian beam of $\lambda = 808$ nm, is impinging on and reflected from the center of the SLM where the dislocation of the phase mask $l\phi$ is programmed, and then it goes to a CCD camera placed in the far-field. Here a picture of the spatial distribution of the diffracted beam is taken.

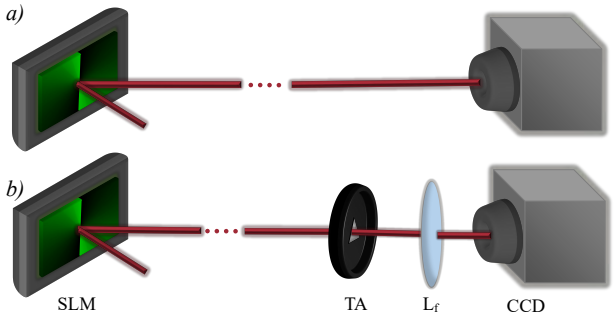

Figure 3.4: (a)Setup for the generation of beams carrying OAM. (b)Setup for the observation of the topological charge.

The setup to directly observe the topological charge is shown in Figure 3.4(b), where, the beam generated previously passes through a triangular aperture (TA) of $500\mu m$ side length. At the TA's plane the size of the beam's central ring is approximately the same as the aperture side length. Then the Fourier transform of the aperture's plane is performed using a 100 mm focal distance lens L_f, and recorded with a CCD camera at the Fourier plane of the lens.

3.4 Type-I Collinear SPDC

The setup for the implementation of the type-I collinear SPDC is depicted in Fig. 3.5(a) where the pump laser beam of wavelength $\lambda_p = 405.2$ nm, is collected by a single mode fiber (SMF) that assures a collimated Gaussian mode with an average power of 50 mW. The polarization is controlled with a half wave plate (HWP) so it is along the extraordinary axis of the crystal (vertical to the optical table), then the beam is focused inside the BBO crystal by a 1000 mm focal distance lense L_f with a beam waist $w_0 = 310$ μm. A high-pass filter and a bandpass filter of $\Delta\lambda = 10$ nm around 808 nm are used to cut off the pump laser wavelength and select the degenerate pair of photons.

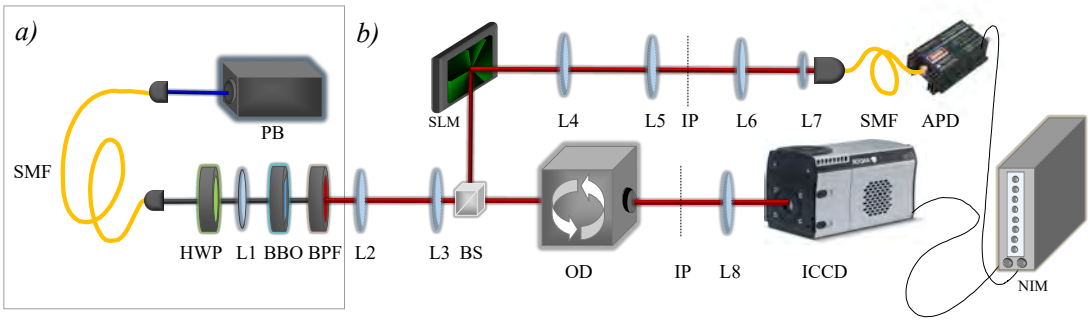

Figure 3.5: (a)Collinear type-I SPDC source. (b)Setup for the OAM mode filter and spatial distribution observation (ICCD picture taken from [27] and APD picture from [28]).

In this part we use a type-I BBO crystal of dimensions $8 \times 8 \times 2\text{mm}^3$, cut so its optical axis is $\theta_p = 29.2°$ with the surface, and for a pump with of wavelength $\lambda_p = 405.2$ nm, the emission angle for the degenerate photons ($\phi_{ei} = \phi_{ei}$) is 3°. As described in section 2.2.2 we can calculate the right angle θ_p to achieve collinear propagation for the degenerated photons. Doing this, the phase matching angle ends up being $\theta_p = 28.8°$, which it is quite close, and collinear emission is achieved by tilting the crystal a little.

3.5 Observation of the Spatial Modes Carrying OAM in Collinear SPDC

As we described previously, SPDC can we written as a superposition of Laguerre-Gauss modes and the pair of photons not only obey energy and linear momentum conservation but also, orbital angular momentum conservation. To observe these modes independently, we need first to filter out the other modes that do not interest us.

Using a beam splitter, the pair of photons (l and $-l$) are separated, one going to a mode discriminator or mode filter (upper branch of Fig. 3.5(b)), and the anti-correlated photon, to the image propagation system where the spatial mode of the photons is going to be observed (lower branch of Fig. 3.5(b)).

In the mode filter, first we image the crystal plane onto the SLM with a $4f$ system, where a spiral phase of topological charge l is set, projecting the photons with topological charge $-l$ into Gaussian modes. Then the SLM plane is re-imaged using a system of 2 telescopes and then coupled into a SMF, filtering out the rest of the higher order modes. The SMF is then connected to an APD where the arrivals of the photons with initial topological charge $-l$ are going to be detected.

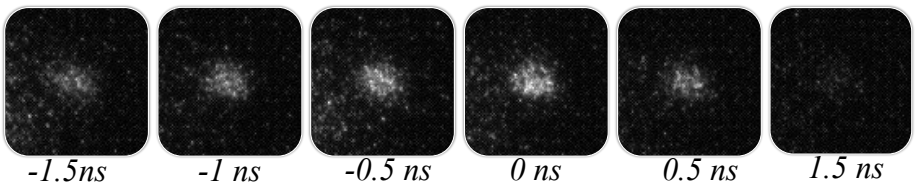

Figure 3.6: Coincidences matching the electronic and optical delay.

In the image propagation system, we propagate the crystal image and send it to an optical delay that is a system composed by 11 telescopes with overall magnification of $M_{od} = 1.5$, with the purpose to compensate for the electronic delay caused by the APD, NIM, etc. until the dashed line in the setup, representing the image plane (IP) of the crystal plane. Then the Fourier transform is performed with a 100 mm focal distance lense L_8, and then goes to an intensified CCD camera, which is triggered by the arrivals of the anti-correlated photon from the mode filter, and in this way the spatial distribution of the mode l is observed.

The Nuclear instrumentation module (NIM) is used as a pulse discriminator and to control the time window to trigger the ICCD camera. It also works as an adjustable electronic delay up to 32 ns in increments of 0.5 ns, feature used for fine delay matching. Fig. 3.6 shows the images in coincidences for the mode $l = 0$ as a function of the delay time, referenced ($t_d = 0$ ns) to the image with highest intensity. The asymmetrical behavior comes from the NIM, since it attenuates the pulse when the delay time set is over 6 ns and that is why it is only used for fine delay matching. For the rest of the electronic delay we use cable. The time window to detect coincidences was set on 12 ns.

The considerations taken in the selection of the lenses for the telescopes are: more efficient phase modulation by the SLM and number of modes coupled into the SMF.

As we can see from Fig. 3.3, for a high value of l the phase modulation is very fast, especially in the center region and the SLM resolution is limited by its pixel size. For very fast modulation the mean phase in the center can be taken constant and no modulation, thus, no OAM is transfered in the center. For that reason, to improve the efficiency of OAM transfer to the mode, we need to increment the beam size. The focal distances are $f_2 = 75$ mm and $f_3 = 250$ mm are used, getting a beam diameter of 2.2 mm.

The next couple of telescopes are chosen to maximize the number of counts detected in the APD and the number of modes we could observe on the ICCD, which was found for a configuration using lenses of focal distances $f_4 = 300$ mm, $f_5 = 60$ mm, $f_6 = 1000$ mm and $f_7 = 8$ mm. Obtaining 4300 counts per second and up to the mode $l = \pm 10$.

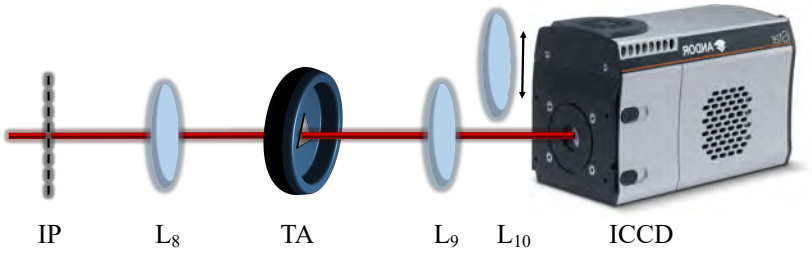

Figure 3.7: Setup for the observation of the OAM of the photons, where the IP symbolizes the image plane in the lower branch of figure 3.5.

3.6 Observation of the Topological Charge Carried by the Photons Produced via Type-I Collinear SPDC

To observe the topological charge we use the same method explained in section 2.1.4 and the setup is shown in Fig. 3.7, where the image plane (IP) of the crystal, where the SPDC is generated, is Fourier transformed and imaged on the triangular aperture (TA) by L_8. As the alignment of the conditional angular spectrum passing through the TA is difficult, a unit magnification telescope (L_9, L_{10}) is used to map the TA plane on the ICCD camera,and a high precision motor (tenths of microns step size) is used to displace the TA until it is centered on the mode singularity as in Fig. 2.4(b). When this is achieved, L_{10} is taken out and the ICCD is moved to the front at the Fourier plane of L_9 ($f_9 = 100$ mm), to observe the diffraction pattern.

This was done for topological charges (l) from ± 1 to ± 2. The focal distance $f_8^{\pm l}$ of L_8 was different for different values of l to fit better the size of the mode to the TA which has 500 μm side length.

$$f_8^{\pm 1} = 250mm,$$
$$f_8^{\pm 2} = 150mm.$$

Chapter 4

Results and analysis

4.1 Generation of Beams Carrying OAM and Observation of Topological Charge

As we mentioned before Laguerre-Gauss modes are also eigenstates of the OAM operator since they have well defined OAM. Thus by adding a spiral phase $l\phi$ to the wavefront and letting it diffract it is expected to end up with a good approximation of a LG mode. More precisely, a superposition of all the LG modes with the same value l, expressed as:

$$LG_l = \sum_{p=0}^{\infty} C_p LG_p. \tag{4.1}$$

Using the experimental setup described in section 3.3, different spatial modes were generated by transferring OAM up to $l = \pm 10$. These spatial modes are shown in Fig. 4.1.

Now, a comparison is made between these modes and the LG modes choosing the first mode for $p = 0$ using Eq. (2.18). In Figure 4.2 a set of plots show the cross-section along the x axis (blue line) and along the y axis (green line) of the spatial modes in 4.1 (up to the mode $l = 6$), are drawn and then compared to the cross section of the simulated LG_{l_0} mode (red line), setting a beam waste of $w_0 = 537\mu m$, and the radial index $p = 0$.

From this, we can see that the central ring radii and the singularity dimensions match. Even though we only used LG_{l_0} modes,we already get a good approximation, and summing over more values of p we can get a better fit to the generated spatial mode. Also we can have the appearance of higher order spiral harmonics, since the spiral phase is not completely linear, due to imperfect calibration and limited SLM

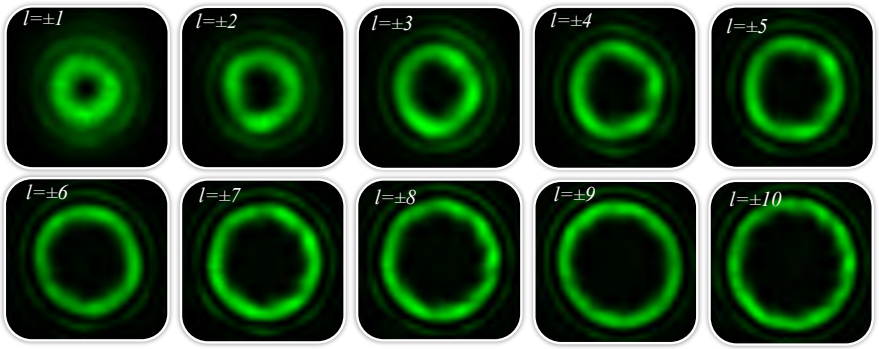

Figure 4.1: Spatial modes carrying OAM generated by adding a spiral phase $l\phi$, for different values of l.

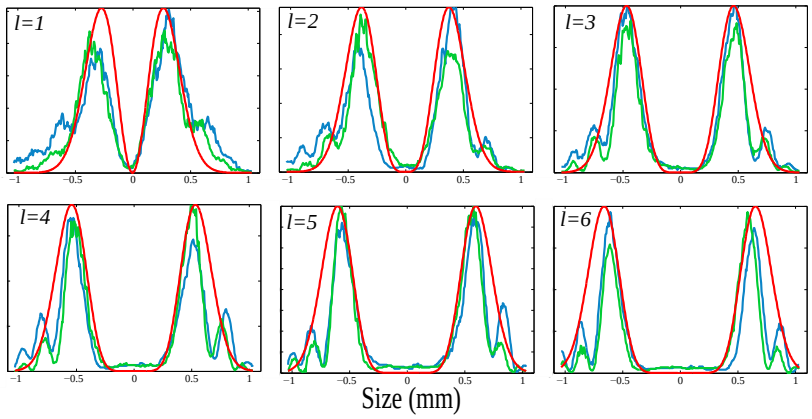

Figure 4.2: Comparison of the cross-section in x (blue line) and y (green line) direction of the spatial modes in 4.1 with a LG_{lp} mode, for $p = 0$ and $l \leq 6$.

resolution.

A bit more complicated holographic patterns are highly used because, in addition to transfer OAM, they can give the desired field amplitude distribution. Since, in this experiment we are only concerned in the value of OAM $\hbar l$ carried by the photons, we make use of the spiral phase-masks generated in the last section.

To prove that the OAM transfer was successful, the method explained in section 3.3 was applied for the same spatial modes generated above, and the results are displayed in Fig. 4.3. In (a) it is done for $l = \pm 1, \pm 2, \pm 3$ and in (b) for $l = \pm 7, \pm 8, \pm 9$. The first column for both cases shows the spatial mode illuminating the triangular aperture, the second and third columns show the diffraction pattern in the far field for the topological charge indicated in the left superior corner. From this, it is noticeable that the spot visibility increases when the size of the central ring illuminates just the edges of the

corners. It can be observed that the rule $l = (N-1)$, N being the number of spots per side, is consistent with the results and also that the $\pm 30°$ rotation tells apart the sign of l, for a counter clockwise rotation corresponds to $l > 0$ and a clockwise rotation to $l < 0$.

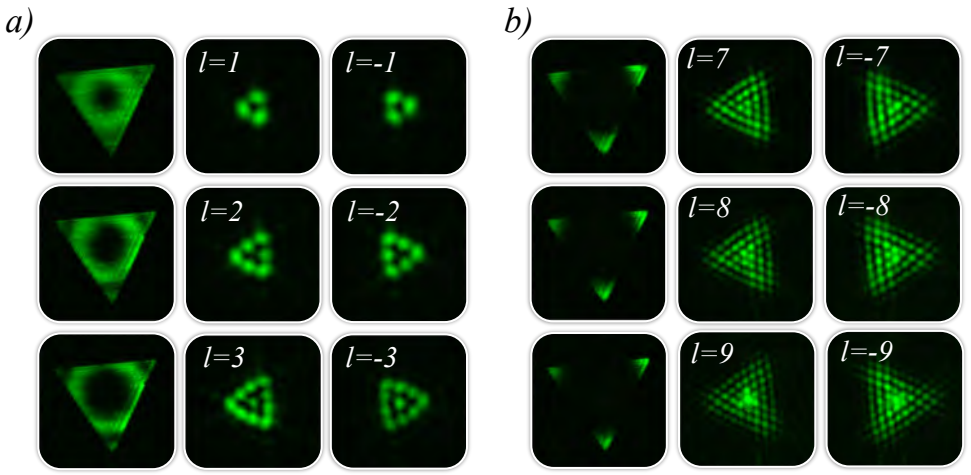

Figure 4.3: Diffraction pattern in the far field of $LG_{l,0}$ mode by a triangular aperture with topological charges (a) $l = \pm 1, \pm 2, \pm 3$ and (b) $l = \pm 7, \pm 8, \pm 9$.

4.2 Spatial Modes Carrying OAM in Type-I Collinear SPDC

Figure 4.4 shows the spatial modes in the far field of the signal photons when the idler photon state $l_i = -l$ is selected, in terms on the size of the modes and coincidences per minute. This is done using the setup explained in section 3.5.

As expected from the selection rule of OAM transfer in type-I collinear SPDC, the spatial mode for $l_i = 0$ is a single spot with a Gaussian intensity profile. For $|l_i| > 0$ spatial modes with ring shaped intensity profile are obtained, where a monotonic growth of the ring radius with $|l_i|$ is observed. This is a property that the spatial modes carrying OAM have.

Spatial modes that have well defined OAM are well represented by LG modes, as we could see in section 4.1. Since we have assumed that LG modes form a complete basis, and that we can discomposed a paraxial field in a superposition of such modes, then we should be able to recover the total conditional angular spectrum of the SPDC.

The last picture in Fig. 4.4 is the superposition of the first 21 modes from $l_i = -10$ to $l_i = 10$. It matches with the Fourier transform of the transversal profile of the pump, which is also a Gaussian mode.

In this section the background noise was taken out by averaging the number of coincidences in the pixels far away from the spatial mode and then subtracted it from all the image and setting the negative values equal to zero.

4.3 Direct Observation of the Topological Carried by Spatial Modes in Type-I Collinear SPDC

The spatial modes in Fig. 4.4 are conformed by the signal photons who are correlated with their respective idler photon which carry topological charge l_i, but they do not say much about the topological charge of the signal photon (apart from the ring radius size). Following the method explained in section 3.6, selecting the state of the idler photon to be $l_i = \pm 1, \pm 2$, we measure the topological charge of the signal photon l_s, and the results are displayed in Fig. 4.5, where the diffraction patterns of the spatial modes are observed. By counting the number of lobes it is evident that $|l_i| = |l_s|$.

Comparing these results with those obtained for the classical $LG_{l,0}$ modes, where a counter clockwise rotation correspond to a positive topological charge $l > 0$, and clockwise rotation for $l < 0$, it is found that by selecting the mode $l_i = l$, the signal photon carries $l_s = -l$. It is proved that the signal photon carries the anti-correlated topological charge of the idler photon, and the selection rule (Eq. (2.55)) holds.

The diffraction pattern for higher values of $|l|$, was not very well observed probably from the flickering defect of the SLM. This is due to voltage fluctuations in the device and it was directly observed in intensity fluctuations of Fig. 4.1 and Fig. 4.3. Since we are using much larger exposure times this defect affects more the measurement. Nevertheless, the results for $|l| = 1, 2$, are well defined and can be extended to higher modes.

4.4 Re-construction of the Entangled Quantum State

As the ICCD records the number of coincidences per pixel, we do not only get information of the mode intensity profile, but also the total number of coincidences by summing over all the pixels, which is a measurement of the probability amplitude coefficients $|C_{\pm l,\mp l}|^2$, given in Eq. (2.59). This allows us to do a quantum tomography and to reconstruct the state. In figure 4.6, the total number of coincidences per minute is shown as a function of l, where it is evident that the probability amplitude decreases

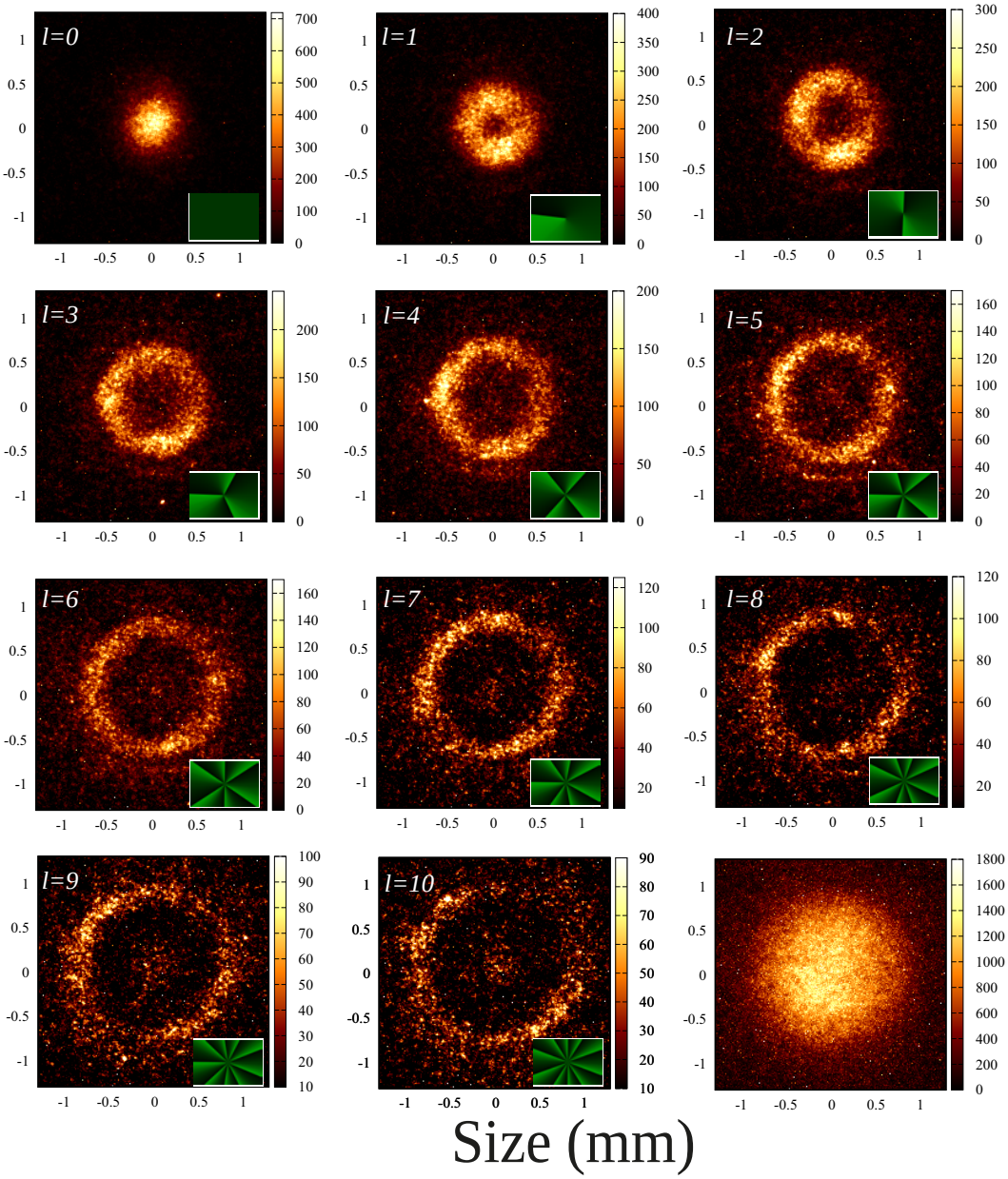

Figure 4.4: Spatial modes of the signal photons when selecting the idler photon in the state $l_i = -l$. On the lower right corner the phase mask of spiral phase $l\phi$ is shown. The last picture represents the superposition of all the first 21 modes ($|l_i| \leq 10$).

the higher order the mode is.

The photons have the same probability of being generated with topological charge l and $-l$,and this means that $|C_{l,-l}|^2 = |C_{-l,l}|^2$ as we discussed in section 2.2.3. In our results, these coefficient decrease monotonically with l and it is centered at $l_i = 0$ as

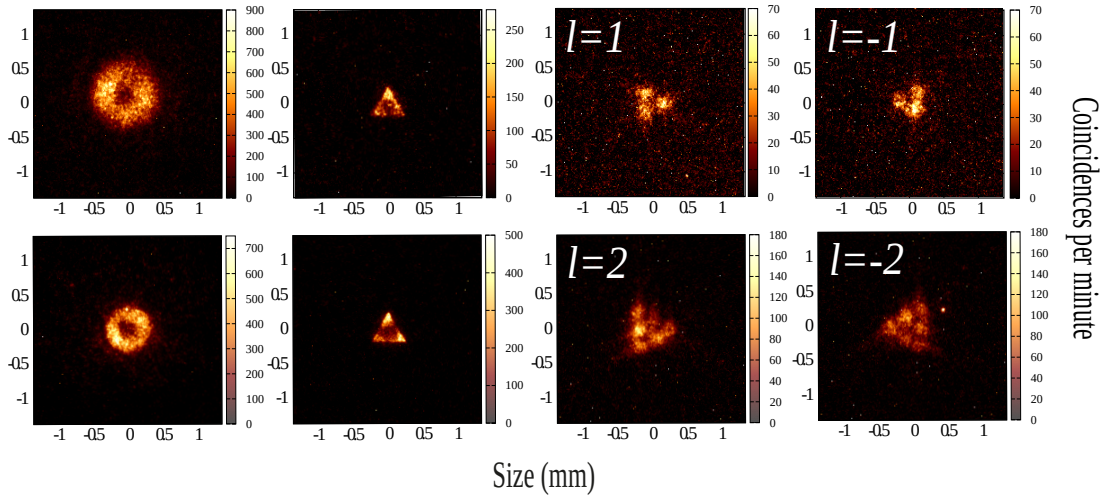

Figure 4.5: First column: Spatial distribution of the photons. Second column: Spatial modes passing through the triangular aperture. Third and Fourth columns: Diffraction pattern of the spatial modes of the photons with topological charge l.

expected. They are shown in Fig. 4.6. Although these coefficients have small discrepancies between each-other, might be due to the coupling in the single mode fibers, since during the experiment realization, it was observed that by changing the phase mask of l for $-l$ an adjustment of the singularity position is needed, meaning that the propagation of these two modes were slightly different. It is known [29] that by using a pump beam with topological charge l_p the behavior would be the same but shifted l_p units.

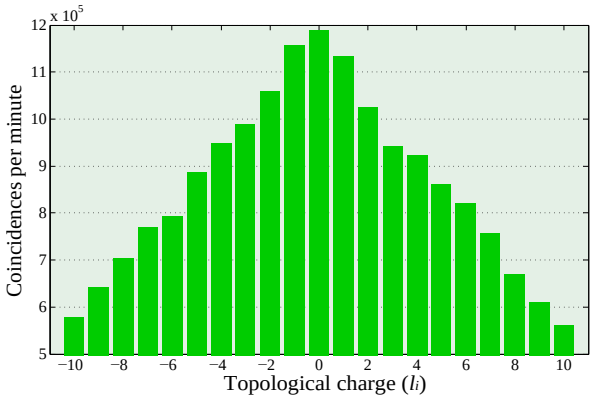

Figure 4.6: Coincidences per minute when selecting idler photon in the state l_i.

Chapter 5

Conclusion and future research work

We implemented a source of pairs of photons that carry Orbital Angular Momentum, and we directly observed and proved that the topological charges which the pair of photons are generated with, meet a selection rule, that states a full transfer of OAM from the pump photon to the idler and signal photons. We can say that, since the state of one photon depends on the state of the other, they are entangled in OAM.

A measurement of the off diagonal probability amplitude coefficients $|l_i\rangle\langle l_s|$, and the displacement of the diagonal elements for different values of the pump beam's topological charge l_p, are left to be done.

One motivation for this project was the use of entangled states in OAM for quantum communications. With our experiment, we now have the tools and techniques to move forward in our research. We now know, how to select the state that we want the other party to measure. Our detection scheme, even though the state measured is obvious to the eye, it is not the appropriate for fast post-processing of the information, besides, it blocks most of the photons, thus requires a long exposure time. Future lines of research include the study of how entangled the system is, and how this entanglement is affected under propagation in a real environment,such is the case for a turbulent atmosphere [10]. Finally, we also wish to perform the same analysis made in this thesis for the propagation of entangled complex structured photons. These are the analogous of the vector vortex beams, that are generated through the superposition of different spatial modes with orthogonal polarization [11]. In appendix A we show the methodology for the experimental implementation of propagation of scalar and vectorial vortex beams in a turbulent atmosphere.

Appendix A

Propagation Through Atmospheric Turbulence

This appendix shows the methodology to simulate a turbulent atmosphere using multi phase-screen approximation. Then we report the results of the propagation in a turbulent atmosphere of a scalar and a radially polarized beams with an amplitude distribution of a Laguerre-Gauss beam $p = 0$ and $l = 1$, calculating the scintillation index as a function of the propagation distance and a comparison with a fundamental Gaussian beam is made.

A.1 Turbulent Atmosphere Simulation Using Multi Phase-screen Approximation

The atmospheric turbulence, due to temperature fluctuations, the refractive index fluctuates randomly from its mean value n_{air}.

$$n(\mathbf{r}) = n_{air} + \delta n(\mathbf{r}), \tag{A.1}$$

where $\langle \delta n(\mathbf{r}) \rangle = 0$. Assuming a beam propagating in $z-$direction through such a medium, it will experience a phase variation from point to point as shown in figure A.1.a and it is given by:

$$\theta(\mathbf{r}) = k_0 \int_0^{\Delta z} \delta n(\mathbf{r}) dz. \tag{A.2}$$

Considering the turbulence to be a locally homogeneous and isotropic, the covariance function of $\delta n(\mathbf{r})$, only depends on the magnitude $r = |\mathbf{r_1} - \mathbf{r_2}|$, rather than the specific coordinates $\mathbf{r_1}$ and $\mathbf{r_2}$:

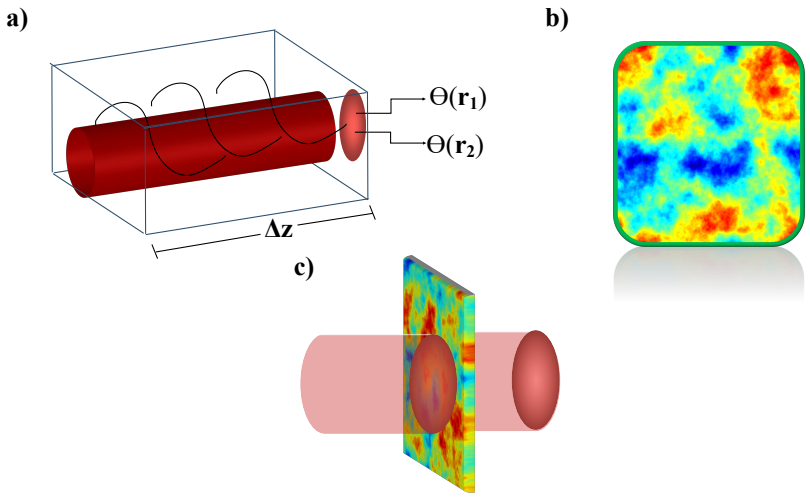

Figure A.1: (a)Beam propagating through a turbulent atmosphere, where the phase from two points after propagation are compared. (b)Phase gained over a propagation distance Δz. (c)Phase-screen approximation.

$$B_n(r) = \langle \delta n(\mathbf{r_1}) \delta n(\mathbf{r_2}) \rangle = \langle \delta n(0) \delta n(r) \rangle. \tag{A.3}$$

From Eq. (A.2) and Eq. (A.3), the covariance function for the phase is given by:

$$B_\theta(r) = \langle \Theta(\mathbf{r_1}) \Theta(\mathbf{r_2}) \rangle = k_0^2 \int \int_0^{\Delta z} \langle \delta n(0) \delta n(r) \rangle dz_1 dz_2. \tag{A.4}$$

Now, the three-dimensional Fourier transform of the covariance function is defined as the *Power Spectrum*.

$$B_n(r) = \frac{1}{(2\pi)^3} \int \int \int_{-\infty}^{\infty} \Phi_n \mathbf{k} e^{-i\mathbf{k}\cdot\mathbf{r}} d^3 r. \tag{A.5}$$

Some models are already established, and particularly for our calculations the *Von-Karman Power Spectrum of the refractive index* was used, which is:

$$\Phi_n(\kappa) = 0.033 C_n^2 e^{-(\frac{\kappa l_0}{5.92})^2} [\kappa^2 + (\frac{2\pi}{L_0})^2]^{-\frac{11}{6}}. \tag{A.6}$$

Here, C_n^2 is called *refractive index structre constant*, which is an indicative of how strong the fluctuations in the refractive index are and for $C_n^2 > 10^{-12} m^{-2/3}$ is said to be a strong turbulence and for $C_n^2 < 10^{-14} m^{-2/3}$ is said to be a weak turbulence. It is a parameter dependent on the height but it can be taken to be constant in horizontal propagation. L_0 represents the *outer scale*, that is the biggest eddie size possible in the

turbulence that breaks up into smaller eddies, which then break up into even smaller eddies until reaching a size l_0, called the *inner scale*, from here they will dissipate through molecular diffusion. This range where the eddies break up from L_0 to l_0 is known as the *inertial range* where Kolmogorov Theory is valid. Von Karman spectrum is a modification of the Kolmorov spectrum, when considering the effects from scales outside the inertial range.

Since the fluctuation of the refractive index is small compared with the mean value $n_{air} >> \delta n(\mathbf{r})$, it allows us to simplify the physics, by assuming $\Delta z >> 1$ in order to obtain a significant perturbation, we can approximate all the phase gained over a distance Δz as a phase-screen as shown in figure A.1(c). Using this approximation and Eqs. (A.3)-(A.6), an expression for the screen-phase can be derived (and shown in figure A.1(b)) [10][30]:

$$\theta_1(\mathbf{R}) + i\theta_2(\mathbf{R}) = \sqrt{2\pi}\frac{k_0}{\Delta_K}\Delta_z^{\frac{1}{2}}\mathcal{F}^{-1}\left\{\tilde{\mathcal{P}}(\mathbf{K})\Phi_n^{\frac{1}{2}}\right\}. \tag{A.7}$$

Here, $\mathbf{R} = x\hat{x} + y\hat{y}$, and the spatial frequency vector $\mathbf{K} = K_x\hat{x} + K_y\hat{y}$. $\tilde{\mathcal{P}}(\mathbf{K})$ is a random complex spectral distribution and k_0 is the wave number of the beam.

A.2 Angular Spectrum Method

For the beam propagation the *angular spectrum method* is used, which considers de beam as a infinite superposition of planes waves [31]:

$$U(x,y,z) = \int\int_{-\infty}^{\infty} A\Big(\frac{\alpha}{\lambda},\frac{\beta}{\lambda},z\Big)exp\Big[j2\pi\Big(\frac{\alpha}{\lambda}x + \frac{\beta}{\lambda}y\Big)\Big], \tag{A.8}$$

where α and β are the direction cosines of the plane waves. Plugging $A(\cdot)$ into the Helmholtz equation can be shown that it admits the solution:

$$A\Big(\frac{\alpha}{\lambda},\frac{\beta}{\lambda},z\Big) = A\Big(\frac{\alpha}{\lambda},\frac{\beta}{\lambda},0\Big)e^{j\frac{2\pi}{\lambda}\sqrt{1-\alpha^2-\beta^2}}. \tag{A.9}$$

From Eq. (A.8) we can see that $A(\cdot)$ is related to $U(\cdot)$ through the Fourier transform, thus:

$$A(x,y,0) = \int\int_{-\infty}^{\infty} U\Big(\frac{\alpha}{\lambda},\frac{\beta}{\lambda},0\Big)exp\Big[-j2\pi\Big(\frac{\alpha}{\lambda}x + \frac{\beta}{\lambda}y\Big)\Big]. \tag{A.10}$$

This way, if we know $U(x,y,0)$, we can calculate $U(x,y,z)$ by applying eqs. A.8-A.10.

A.3 Cylindrical Vector Beams

Vector Beams (VB) are the solution of the vector electromagnetic wave equation where the polarization distribution of the transverse profile of the beam varies from point to point on the wave-front. Cylindrical Vector Beams (CVB) are the family of VB with axial symmetry. Most known CVB's are the Radial and Azimuthal polarization. The relevancy of these two types of beams, specially the former, is mainly due to their focusing properties and their application in high resolution microscopy, 3D focus shaping, particle Trapping , lithography, etc.

The superposition of orthogonal cylindrical scalar beams can produce the CVB beams with interesting polarization distributions. Using two arbitrary LG modes one with right circular polarization (RCP) and the other with left circular polarization(LCP), and a phase delay ϕ_0 with respect to each other, we can write this superposition as:

$$\vec{E}(\vec{r}) = E_p^{|l|} e^{i(l\phi+\phi_0/2)}(\hat{x} + i\hat{y}) + E_{p'}^{|l'|} e^{il'(\phi-\phi_0/2)}(\hat{x} - i\hat{y}). \tag{A.11}$$

Here,$E_p^{|l|} e^{il\phi} = LG_p^l$. For the case $l' = -l$,

$$\vec{E}(\vec{r}) = 2 \cdot E_p^{|l|}(\cos(l\phi + \phi_0/2)\hat{x} - \sin(l\phi + \phi_0/2)\hat{y}). \tag{A.12}$$

From (A.12) we can see that the OAM is no longer encoded in the phase since there is no helical phase anymore, but instead, it is encoded in the polarization distribution. Figure A.2 show the polarization patterns for different values of l, l' and ϕ_0. The first image is know as Poincaré Beam, since contains all the degrees of polarizations. From the second and third image we see that from the superposition of $l = 1$ and $l' = -1$, we obtain radial and azimuthal polarization choosing ϕ_0 to be 0 and π respectively.

A.4 Numerical Method

To create the single phase screen, we assumed a beam wavelength $\lambda = 2$ μm, an outer scale $L_0 = 3$ m, the inner scale $l_0 = 10$ mm, we considered $C_n^2 = 10^{-12} m^{-2/3}$ for strong turbulence and $C_n^2 = 10^{-14} m^{-2/3}$ for weak turbulence. The random complex spectral field $\tilde{\mathcal{P}}(\mathbf{K})$, is generated through filtering Gaussian noise using MATLAB, creating an array of 512×512 elements $A + iB$.

The phase-screen is multiplied to the field and then propagated using the angular spectrum method, then repeated in intervals of $\Delta_z = 100$ m as shown in fig. A.3.

The study of beam propagation through a turbulent atmosphere was done for 3 different kind of beams: a Scalar Vortex Beam (SVB), chosen to be a LG with topological charge $l = 1$ and radial index $p = 0$, a Vector Vortex beam (VVB) radially

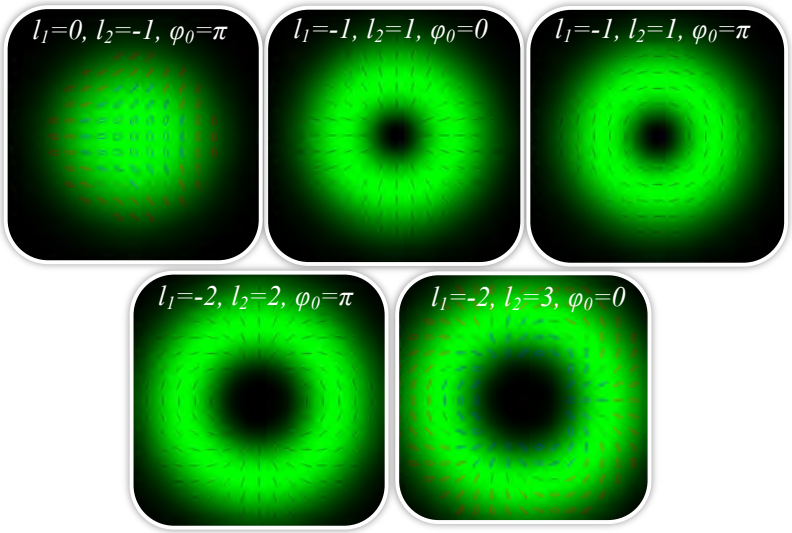

Figure A.2: Cylindrical vector beams for different values of l, l' and ϕ. First:Poincare beam. Second: Radially polarized beam. Third: Azimuthally polarized beam.

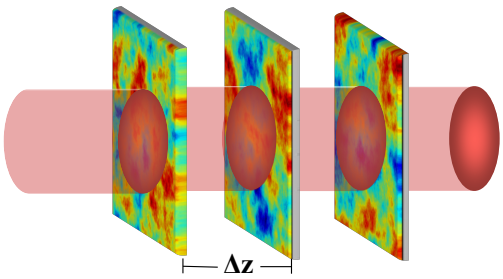

Figure A.3: Multi phase-screen approximation.

polarized and the same transverse intensity profile than the SVB, and finally a fundamental Gaussian beam.

The beams were generated using the equation:

$$E_l(r) = \left(\frac{\sqrt{2}r}{w_0}\right)^l L_l^p e^{(-r^2/w_0^2 + il\phi)}. \tag{A.13}$$

Here, L_l^p is the associated Laguerre polynomial, w_o is the beam waist. With $l = 0, p = 0$ we obtain the Gaussian beam (GB), choosing $l = 1$, $p = 0$ we get the SVB and finally, the radially polarized VVB was manage through $(E_{-l} + E_l)/2$.

Three aspects of the beams were studied: The average intensity profile, the scintillation index and finally, the polarization evolution of the VVB.

A.5 Results and Analysis

A.5.1 Average Intensity Profile

Here we observe the intensity profile of the respective beam after propagating a distance Z through the atmosphere. Since the turbulence is a random process, the beam intensity profile is never the same for different realizations of the propagation, and for this reason, the average over an ensemble of 500 realizations was taken.

Figures. A.4-A.6 show the results for the GB, SVB and VVB respectively. For the case of GB, as expected the beam spreads out much faster in a strong turbulence a deformation from the Gaussian shape of the intensity starts to become visible from $Z = 100$ m, while in the weak turbulence regime it does not seem to expand much as it propagates and the deformation from the Gaussian profile is barely visible at $Z = 2000$ m.

The SVB and the VVB intensity profiles behaves the same way, they spread out until the singularity is lost which happens in somewhere between $Z = 600$ m and $Z = 700$ m for both in strong turbulence. After this, it continues expanding as a Gaussian beam. In weak turbulence at $Z = 2000$ m the singularity still persists with a visibility $V = 0.52$.

For the case of GB, as expected, the beam spreads out much faster in a strong turbulence a deformation from the Gaussian shape of the intensity starts to become visible from $Z = 100$ m, while in the weak turbulence regime it does not seem to expand much as it propagates and the deformation from the Gaussian profile is barely visible at $Z = 2000$ m.

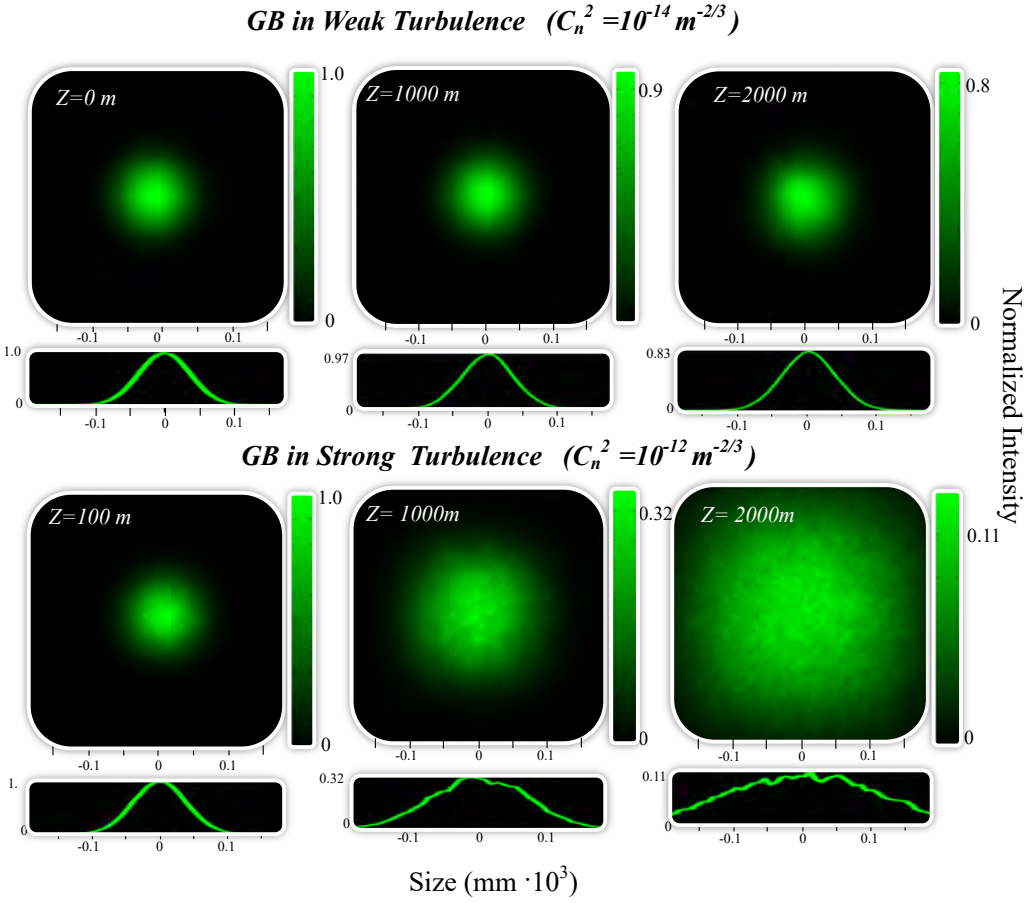

Figure A.4: Average intensity profile of a fundamental Gaussian beam after a propagation Z in atmospheric turbulence.

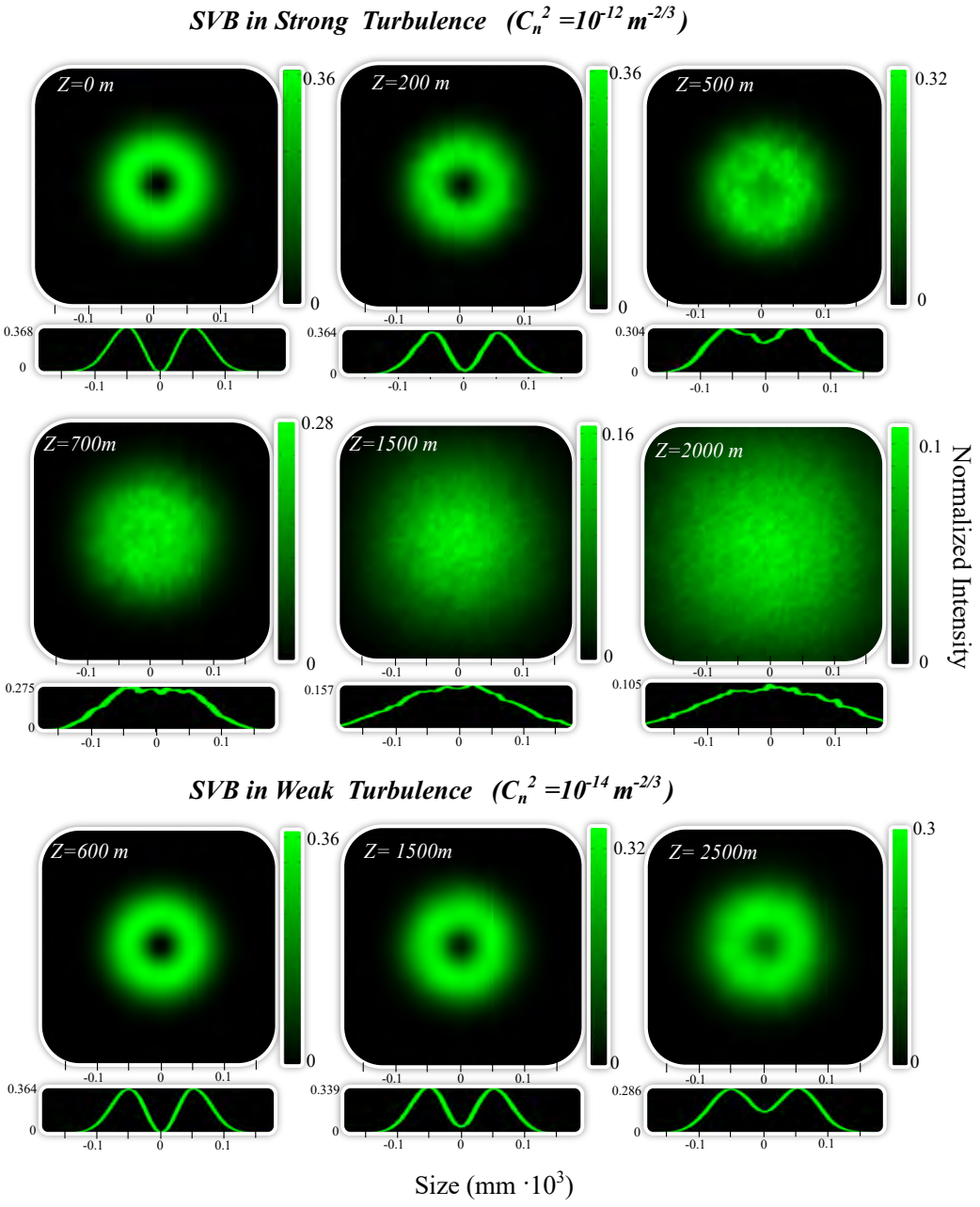

Figure A.5: Average intensity profile of a scalar vortex beam, LG_1^0, after a propagation Z in atmospheric turbulence.

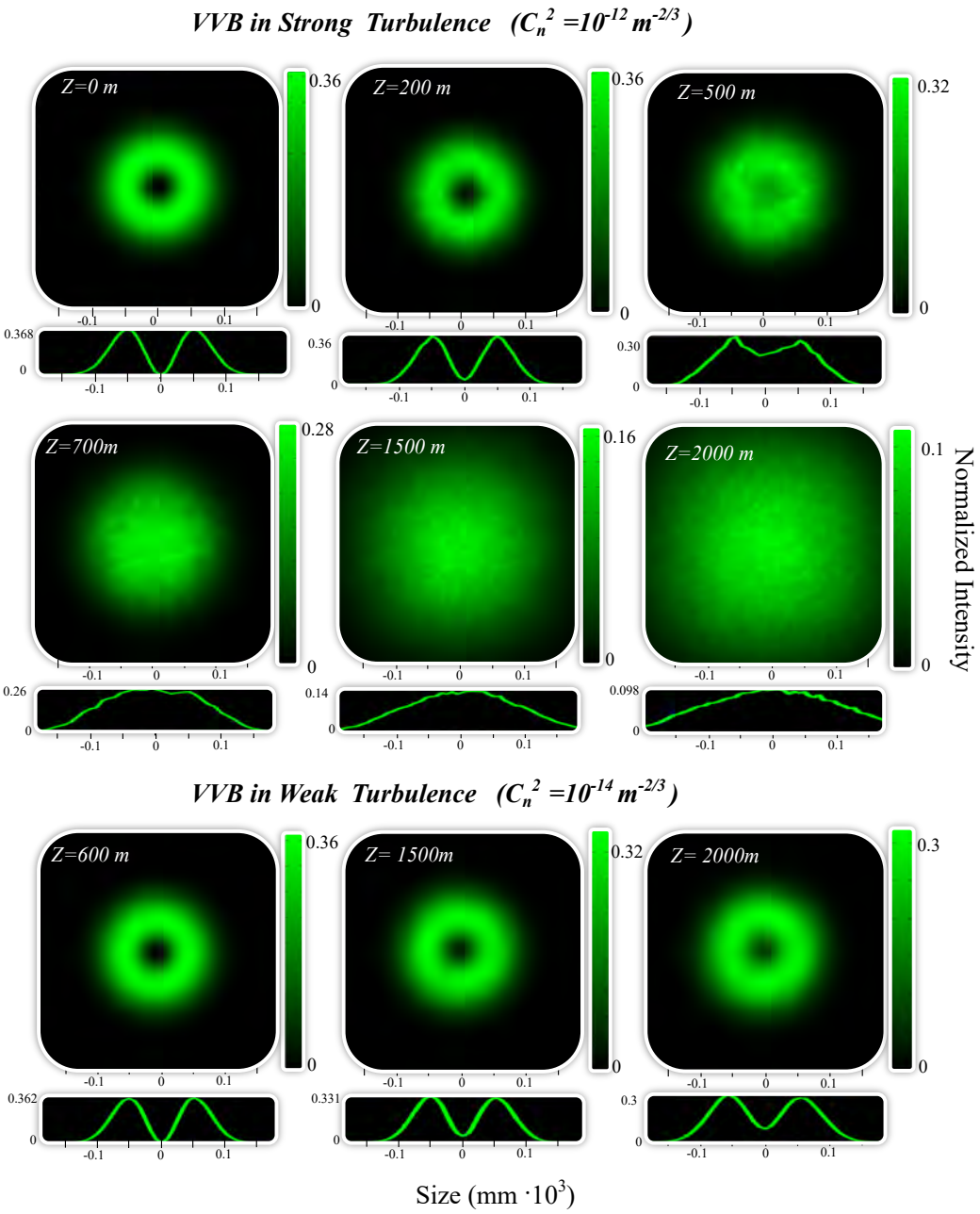

Figure A.6: Average intensity profile of a radially polarized vector vortex beam, after a propagation Z in atmospheric turbulence.

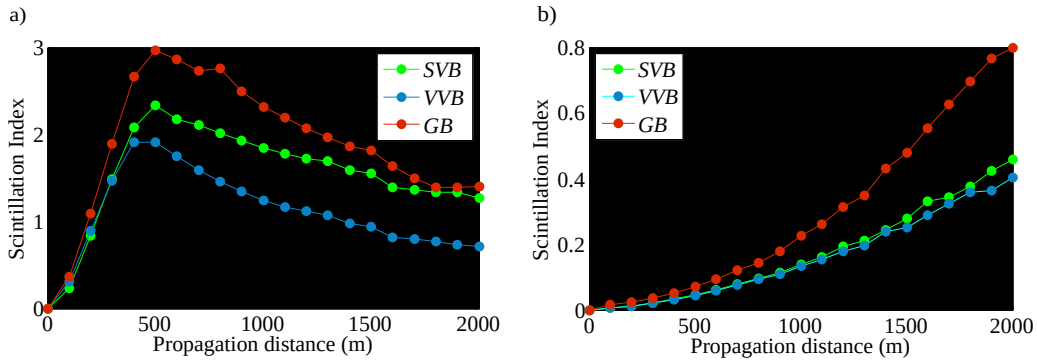

Figure A.7: Scintillation index as a function of the propagation distance for (a) Strong turbulence $C_n^2 = 10^{-12}m^{-2/3}$ and (b) strong turbulence

The SVB and the VVB intensity profiles behaves the same way, they spread out until the singularity is lost which happens in somewhere between $Z = 600$ m and $Z = 700$ m for both in strong turbulence. After this, it continues expanding as a Gaussian beam. In weak turbulence at $Z = 2000$ m the singularity still persists with a visibility $V = 0.52$.

A.5.2 Scintillation Index

Another useful parameter in the study of light propagation through a turbulence medium, is the scintillation index (SI), which is defined as the variance of the intensity of the beam,which is related to the distortion of the phase.The SI is given by:

$$\sigma_I = \frac{\langle I^2 \rangle \langle I \rangle^2}{\langle I \rangle^2} \tag{A.14}$$

Same as before, the ensemble average was taken over 500 realizations. To give a good comparison an annular width of $(1 \pm 5\%)w(z)$ around the beam waist $w(z)$ was taken into account for the calculation of SI to ensure there are sufficient number of data. Figure A.7(a) shows the result for the 3 beams in a weak turbulence , and figure A.7(b) shows it for a strong turbulence.

From these results we see that the intensity fluctuation a lower for the VVB even specially in the strong turbulence regime, suggesting to be more robust against turbulence than the SVB, even though they have almost the same intensity profile.

A.5.3 Polarization Evolution of the VVB

In this part we observe the polarization evolution of the VVB by looking at the stokes parameters S_1 and S_3, and the *degree of polarization* (DOP). Here the points where

the normalized intensity $S_0 \geq 10^{-5}$ were taken into account. We also display the polarization distribution (PD), where the green straight lines represents linear polarization and red and and blue ellipses represent right and left elliptical polarization, respectively.

The expressions for DOP, S_1 and S_3 are:

$$S_0 = |E_x|^2 + |E_y|^2, \tag{A.15}$$

$$S_1 = \frac{|E_x|^2 - |E_y|^2}{S_0}, \tag{A.16}$$

$$S_2 = \frac{2|E_x||E_y|cos\delta}{S_0}, \tag{A.17}$$

$$S_3 = \frac{2|E_x||E_y|sin\delta}{S_0}, \tag{A.18}$$

where δ is the phase between the E_x and E_y. From figure A.8 observe a singularity in DOP and S_1 at the center at any distance Z, and that they both are decreasing from the center to the edges as the beam propagates. Also, S_3 develops random values from point to point, same for S_1 at the center.

This tells us that the beam is depolarizing. Figure A.9 shows a section of the polarization distribution at $Z = 1500$ m, where it is noticeable an unpolarized region that belongs to the center of the beam (lower right corner), but as we moving away from it we see that it gets more polarized.

Figure A.10 shows the same parameter at $Z = 2000$ m for strong (first row) and weak (second row) turbulence, where we still find partially polarized light, although this corresponds to a zone of low intensity.

A.6 Conclusion

From the results, it is apparent that vector vortex beams are more robust against turbulence than the scalar vortex beams, for a couple of things. Apart from having a lower intensity fluctuation, the VVB presents a vectorial vortex in the polarization at $Z = 2000$ m, even though they both lose the singularity in the intensity at around $Z = 700m$. Also, in optical communication using Orbital Angular Momentum as a degree of freedom for information codification, since OAM is coded in the phase of the beam, it is highly susceptible to atmospheric turbulence. As we mentioned before in section A.3, using VVB's, one can code the OAM information in the polarization distribution of the beam which has more robustness against turbulence, and the information of the topological charges of the beams composing the VVB can be extracted easily.

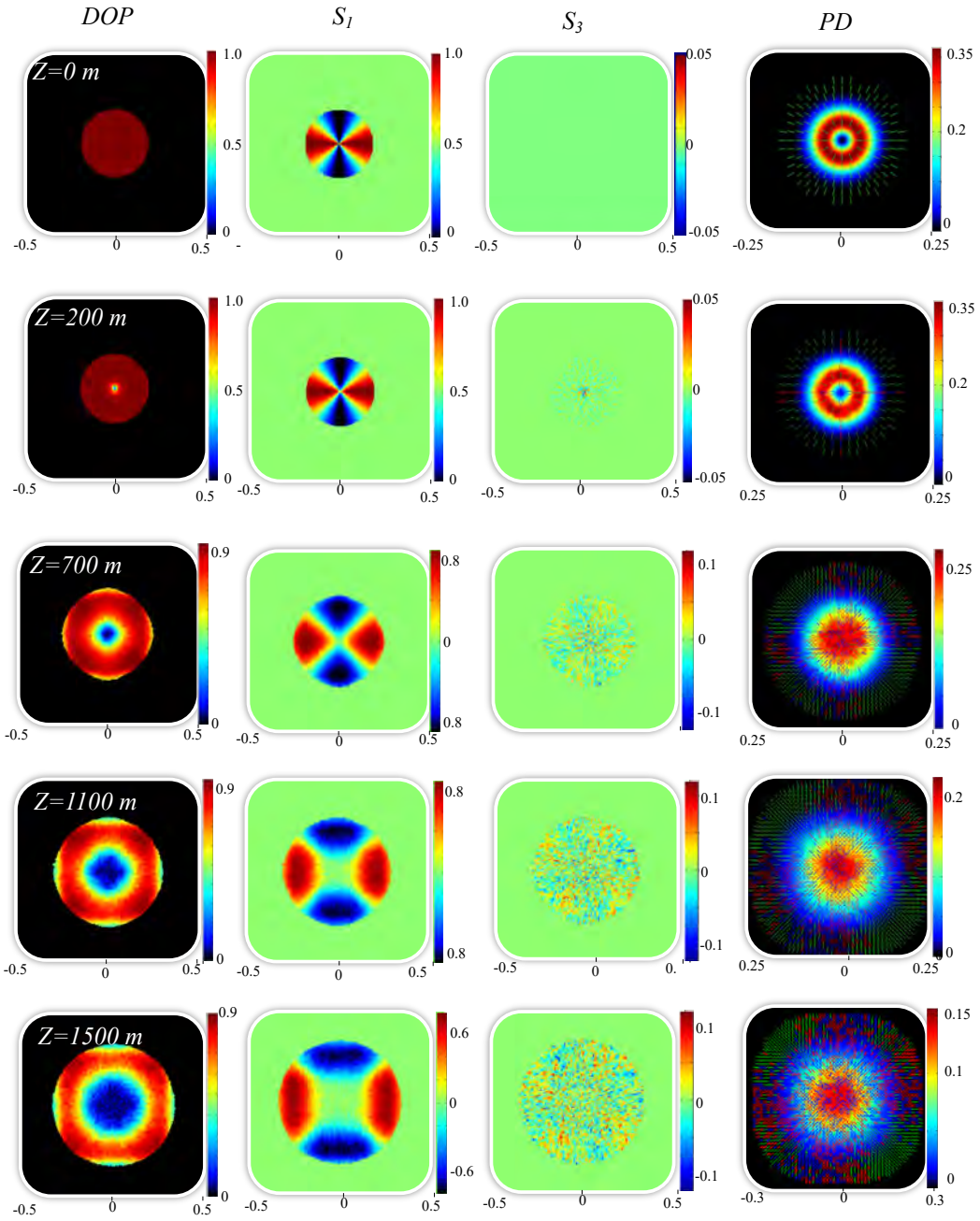

Figure A.8: First column shows the degree of polarization, the second column the S_1, the third column shows S_3 and finally the fourth column depicts the polarization distribution at different propagation distances.

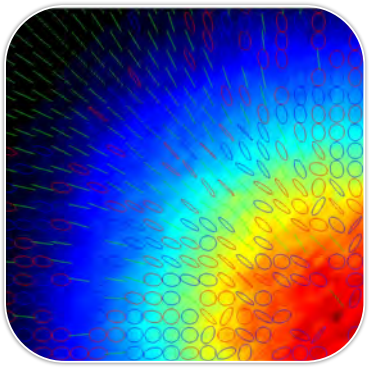

Figure A.9: Zoom in of the polarization distribution at $Z = 1500$ m, showing the unpolarized region and the partially polarized region.

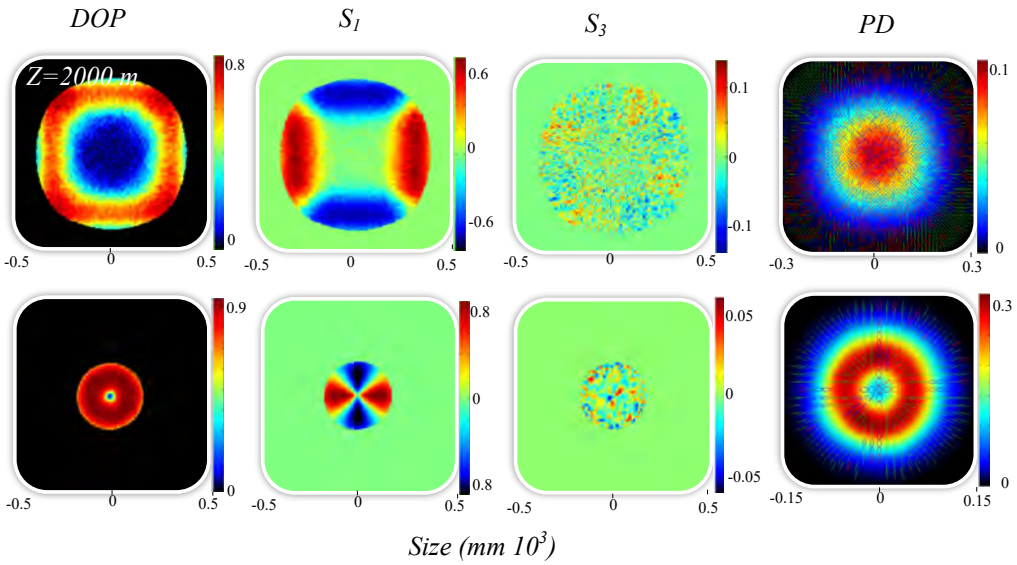

Figure A.10: Comparison of DOP, S_1, S_2 and PD in both regimes, strong (first row) and weak (second row) at $Z = 2000$ m.

Bibliography

[1] L. Allen, M. W. Beijersbergen, R.J. Spreeuw, and J. P. Woerdan. *Orbital angular momentum of light and the transformation of Laguerre-Gaussian laser modes.* Phys. Rev. A**45**, 8185 (1992). 3

[2] Miles G. Padgett. *Orbital angular momentum 25 years on.* Opt. Exp. **25**, 11265 (2015). 3

[3] A. E. Willner, H. Huang, Y. Yan, Y. Ren, N. Ahmed, G. Xie, C. Bao, L. Li, Y. Cao, Z. Zhao, J. Wang, M. P. J. Lavery, S. Ramachandran M. Tur, A. F. Molisch, N. Ashrafi, and S. Ashrafi. *Optical communications using orbital angular momentum beams.* OSA Pub. **7**, 66-106 (2015). 3

[4] C. H. Bennett and G. Brassard. *Quantum Cryptography: Public key distribution and coin tossing.* Theoretical Computer Science **5607**-11 (2014). 3

[5] Sheng-Kai Liao, Wen-Qi Cai, Johannes Handsteiner, Bo Liu, Juan Yin, Liang Zhang, Dominik Rauch, Matthias Fink, Ji-Gang Ren, Wei-Yue Liu, et al. *Satellite-relayed intercontinental quantum network.* Phys. rev. letters **120** 030501 (2018). 3

[6] Frédéric Bouchard, Khabat Heshami, Duncan England, Robert Fickler, Robert W. Boyd, Berthold-Georg Englert, Luis L. Sánchez-Soto, and Ebrahim Karimi. *Experimental investigation of high-dimensional quantum key distribution protocols with twisted photons.* arXiv:1802.05773v2 (2018). 3

[7] Adetunmise C. Dada, Jonathan Leach, Gerald S. Buller, Miles J. Padgett, and Erika Andersson. *Experimental high-dimensional two-photon entanglement and violations of generalized Bell inequalities.* Nature Physics volume **7**, 677–680 (2011). 3

[8] Krenn M, Flicker R., Sven Ramelow, Radek Lapkiewicz, and Zeilinger A. *Real-time imaging of quantum entanglement.* Scientific Reports **3**, 1914 (2013) . 3

[9] Robert Flicker. *Quantum Entanglement of Complex Structures of Photons.* PhD thesis, University of Vienna, Austria, 2016. 4

[10] A. Hamadou Ibrahim, Filippus S. Roux, Melanie McLaren, Thomas Konrad, and Andrew Forbes. *Orbital angular momentum entanglement in turbulence.* Phys. Rev. A **88**, 012312 (2013). 4, 37, 41

[11] Alicia Sit, andJeremie Gagnon-Bischoff Robert Flicker, Hugo Larocque, R. Boyd, and Ebrahim Karimi. *High-dimensional intracity quantum cryptography with structured photons.* Optica Vol.**4** 1006-1010 (2017). 4, 37

[12] Mario Krenna, Johannes Handsteinera, Matthias Finka, Robert Fickler, and Anton Zeilinger. *Twisted photon entanglement through turbulent air across Vienna.* PNAS **112**, 14197–14201 (2015). 4

[13] Krenn M, Malik M, Erhard M, and Zeilinger A. *Orbital angular momentum of photons and the entanglement of Laguerre–Gaussian modes.* Phil. Trans. R. Soc. A **375**, 20150442 . 4

[14] R. S. Aspden, D. S. Tasca, R. W. Boyd, and M. J. Padgett. *EPR-based ghost imaging using a single-photon-sensitive camera.* New J. Phys. 15, 073032 (2013). 4

[15] D. L. Andrews and M. Babiker. *The Angular Moment of Light.* Cambridge University Press, Cambridge, 2013. 7, 9

[16] W.C Soares J.M. Hickmann, E.J.S. Fonseca and S. Chávez-Cerda. *Unveiling a Truncated Optical Lattice Associated with a Triangular Aperture Using Light's Orbital Angular Momentum.* Phys. Rev. Lett. **105**, 053904 (2010). 12

[17] R. W. Boyd. *Nonlinear Optics Third Edition.* Academic Press, Chicago, 2008. 13, 14, 17

[18] Peter E. Powers and Joseph W. Haus. *Fundamentls of Non-Linear Optics 2nd Edition.* CRC Press, Boca Raton, FL, 2017. 14, 15

[19] D. N. Klyshko. *Scattering of light in a medium with nonlinear polarizabilty.* Zh. Eksp. Teor. Fiz. **55** 1006-1013 (1968) . 16

[20] C. C. Gerry and P. L. Knigth. *Introductory Quantum Optics.* Cambridge University Press, New York, 2005. 17

[21] J. J. Sakurai. *Modern Quantum Mechanics.* Addison Wesley Publishing, USA, 1994. 17

[22] Clara Ines Osorio Tamayo. *Spatial Characterization of Two-Photon States.* PhD thesis, ICFO, Barcelona, 2009. 17, 20

[23] Hector Cruz Ramírez. *Acondicionamiento del enredamiento espacial en parejas de fotones producidas por conversion parametrica descendente.* PhD thesis, UNAM, Mexico. 18

[24] Clara Osorio, G Molina-Terriza, and Juan P Torres. *Orbital angular momentum correlations of entangled paired photons.* Pure Appl. Opt. **11**, 094013 (2009) . 19, 20

[25] Wei Han, Yanfang Yang, Wen Cheng, , and Qiwen Zhan. *Vectorial optical field generator for the creation of arbitrarily complex fields.* Opt. Express **21**, 20692-20706 (2013). 23, 24

[26] thorlabs.us. 24

[27] directindustry.es. 27

[28] digikey.com. 27

[29] A. Mair, A. Vaziri, G. Weihs, and A. Zeilinger. Entanglement of the orbital angular momentum states of photons. Nature **412**, 313-316 (2001). 36

[30] Wen Cheng, Joseph W. Haus, and Qiwen Zhan. *Propagation of vector vortex beams through a turbulent atmosphere.* Opt. Express **17**, 17835 (2009). 41

[31] Joshep W. Goodman. *Introduction to Fourier Optics.* Roberts and Company Publishers (2007). 41